Since January 2020 Elsevier has created a COVID-19 resource centre with free information in English and Mandarin on the novel coronavirus COVID-19. The COVID-19 resource centre is hosted on Elsevier Connect, the company's public news and information website.

Cell Reports

Article

A Fc-enhanced NTD-binding non-neutralizing antibody delays virus spread and synergizes with a nAb to protect mice from lethal SARS-CoV-2 infection

Graphical abstract

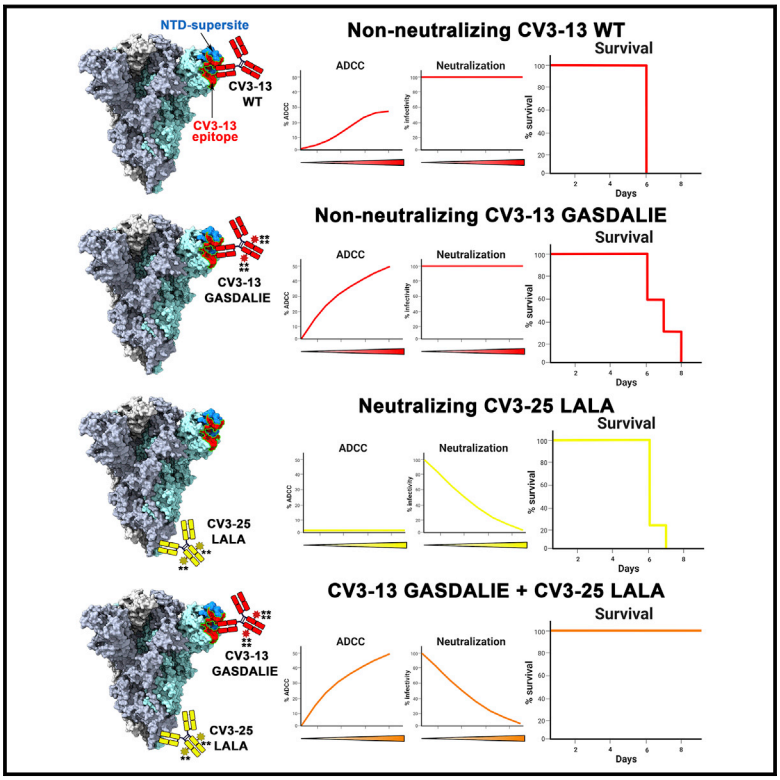

Highlights

- Non-neutralizing antibody CV3-13 binds an epitope in NTD of SARS-CoV-2 spike
- CV3-13 has a unique angle of approach and mediates potent Fc-effector functions
- Fc-enhanced CV3-13 delays virus spread and death in SARS-CoV-2-challenged mice
- Fc-enhanced CV3-13 synergizes with Fc-compromised nAb to protect 100% of the mice

Authors

Guillaume Beaudoin-Bussières, Yaozong Chen, Irfan Ullah, ..., Pradeep D. Uchil, Marzena Pazgier, Andrés Finzi

Correspondence

pradeep.uchil@yale.edu (P.D.U.), marzena.pazgier@usuhs.edu (M.P.), andres.finzi@umontreal.ca (A.F.)

In brief

The *in vivo* impact of non-nAbs on SARS-CoV-2 infection is unclear. Here, Beaudoin-Bussières et al. show that a Fc-enhanced version of non-nAb CV3-13 delays SARS-CoV-2 spread and death in mice. Fc-enhanced CV3-13 combined with a Fc-compromised nAb synergizes to protect mice, revealing the importance of non-nAbs during SARS-CoV-2 infection.

Beaudoin-Bussières et al., 2022, Cell Reports *38*, 110368
February 15, 2022
https://doi.org/10.1016/j.celrep.2022.110368

CellPress

Cell Reports

CellPress
OPEN ACCESS

Article

A Fc-enhanced NTD-binding non-neutralizing antibody delays virus spread and synergizes with a nAb to protect mice from lethal SARS-CoV-2 infection

Guillaume Beaudoin-Bussières,[1,2,14] Yaozong Chen,[3,14] Irfan Ullah,[4,14] Jérémie Prévost,[1,2] William D. Tolbert,[3] Kelly Symmes,[4] Shilei Ding,[1] Mehdi Benlarbi,[1] Shang Yu Gong,[1,5] Alexandra Tauzin,[1,2] Romain Gasser,[1,2] Debashree Chatterjee,[1] Dani Vézina,[1] Guillaume Goyette,[1] Jonathan Richard,[1,2] Fei Zhou,[13] Leonidas Stamatatos,[6,7] Andrew T. McGuire,[6,7,8] Hughes Charest,[9] Michel Roger,[1,2,9] Edwin Pozharski,[11,12] Priti Kumar,[4] Walther Mothes,[10] Pradeep D. Uchil,[10,*] Marzena Pazgier,[3,*] and Andrés Finzi[1,2,5,15,*]

[1]Centre de recherche du CHUM, Montreal, QC H2X 0A9, Canada
[2]Département de Microbiologie, Infectiologie et Immunologie, Université de Montréal, Montreal, QC H2X 0A9, Canada
[3]Infectious Disease Division, Department of Medicine, Uniformed Services University of the Health Sciences, Bethesda, MD 20814-4712, USA
[4]Department of Internal Medicine, Section of Infectious Diseases, Yale University School of Medicine, New Haven, CT 06520, USA
[5]Department of Microbiology and Immunology, McGill University, Montreal, QC H3A 2B4, Canada
[6]Vaccine and Infectious Disease Division, Fred Hutchinson Center, Seattle, WA 98195, USA
[7]Department of Global Health, University of Washington, Seattle, WA 98195, USA
[8]Department of Laboratory Medicine and Pathology, University of Washington, Seattle, WA 98195, USA
[9]Laboratoire de Santé Publique du Québec, Institut national de santé publique du Québec, Sainte-Anne-de-Bellevue, QC H9X 3R5, Canada
[10]Department of Microbial Pathogenesis, Yale University School of Medicine, New Haven, CT 06510, USA
[11]University of Maryland Institute for Bioscience and Biotechnology Research, Rockville, MD 20850, USA
[12]Department of Biochemistry and Molecular Biology, University of Maryland School of Medicine, Baltimore, MD 21201, USA
[13]Division of Basic and Translational Biophysics, Unit on Structural Biology, NICHD, NIH, Bethesda, MD 20892, USA
[14]These authors contributed equally
[15]Lead contact
*Correspondence: pradeep.uchil@yale.edu (P.D.U.), marzena.pazgier@usuhs.edu (M.P.), andres.finzi@umontreal.ca (A.F.)
https://doi.org/10.1016/j.celrep.2022.110368

SUMMARY

Emerging evidence indicates that both neutralizing and Fc-mediated effector functions of antibodies contribute to protection against SARS-CoV-2. It is unclear whether Fc-effector functions alone can protect against SARS-CoV-2. Here, we isolated CV3-13, a non-neutralizing antibody, from a convalescent individual with potent Fc-mediated effector functions. The cryoelectron microscopy structure of CV3-13 in complex with the SARS-CoV-2 spike reveals that the antibody binds from a distinct angle of approach to an N-terminal domain (NTD) epitope that only partially overlaps with the NTD supersite recognized by neutralizing antibodies. CV3-13 does not alter the replication dynamics of SARS-CoV-2 in K18-hACE2 mice, but its Fc-enhanced version significantly delays virus spread, neuroinvasion, and death in prophylactic settings. Interestingly, the combination of Fc-enhanced non-neutralizing CV3-13 with Fc-compromised neutralizing CV3-25 completely protects mice from lethal SARS-CoV-2 infection. Altogether, our data demonstrate that efficient Fc-mediated effector functions can potently contribute to the *in vivo* efficacy of anti-SARS-CoV-2 antibodies.

INTRODUCTION

Several vaccine platforms have been approved in different jurisdictions worldwide to counter the COVID-19 pandemic (Oliver et al., 2021a, 2021b; Polack et al., 2020; Voysey et al., 2021) with vaccine development primarily focused on generating immune responses against the SARS-CoV-2 spike. The spike mediates viral entry and is well exposed at the surface of virions (Duan et al., 2020; Shang et al., 2020) and infected cells ((Ding et al., 2021)Buchrieser et al., 2020). The spike is a trimer of heterodimers, composed of two subunits, S1 and S2, generated by furin cleavage. The S1 subunit permits attachment via its receptor binding domain (RBD) to the cellular receptor angiotensin converting enzyme 2 (ACE2) (Hoffmann et al., 2020; Lan et al., 2020; Walls et al., 2020; Wrapp et al., 2020b). It also contains an N-terminal domain (NTD) that may aid attachment and conformational transition of spike, as observed for other coronaviruses (Amraie et al., 2020; Lempp et al., 2021; Soh et al., 2020). Considerable effort has been made to study antibody-mediated neutralization and its effect in mitigating SARS-CoV-2 infection. Many neutralizing antibodies target the RBD, but some targeting the NTD and the S2 subunits were reported (Cao et al., 2020;

Chen et al., 2020; Chi et al., 2020; Jennewein et al., 2021; Ju et al., 2020; Li et al., 2021b; Liu et al., 2020; Rappazzo et al., 2021; Seydoux et al., 2020; Suryadevara et al., 2021; Ullah et al., 2021a; Voss et al., 2021; Wang et al., 2020; Wrapp et al., 2020a; Wu et al., 2020b; Yuan et al., 2020). Some studies have shown that around 25%–45% of people who resolve the infection have plasma with low or undetectable levels of SARS-CoV-2 neutralizing activity (Beaudoin-Bussieres et al., 2020; Luchsinger et al., 2020; Muecksch et al., 2021; Payne et al., 2020; Prevost et al., 2020; Robbiani et al., 2020; Wu et al., 2020a). Moreover, recent studies have shown that, despite a significant loss in neutralizing activity against the B.1.1.7 (Alpha) and B.1.351 (Beta) variants, the AstraZeneca and Pfizer/BioNTech vaccines remain efficacious against these variants (Emary et al., 2021; Pfizer/BioNTech, 2021). These data suggest that immune functions of antibodies beyond neutralization may play a role in SARS-CoV-2 control.

The antigen binding domain (Fab) of antibodies is critical for neutralization but the crystallizable fragment (Fc) of the antibody can contribute significantly to their *in vivo* efficacy (Bournazos et al., 2019; Bournazos et al., 2014; DiLillo et al., 2014). Fc engagement of Fc gamma receptors (FcγRs) elicits complement-dependent cytotoxicity, antibody-dependent cellular cytotoxicity (ADCC) and antibody-dependent cellular phagocytosis (ADCP) depending on the effector cell to which they bind. We previously examined the protection mediated by neutralizing antibodies (nAbs) targeting the SARS-CoV-2 spike in a K18-hACE2 mouse model and the effect of wild-type (WT) or Fc-mutated versions in a prophylactic or therapeutic setting (Ullah et al., 2021a). The Fc mutations (L234A-L235A [LALA]), significantly diminished the affinity of antibodies to FcγRIIIa and also impacted Fc-mediated effector functions. Interestingly, in this study we showed LALA mutations significantly diminished the capacity of nAbs to protect mice from a lethal SARS-CoV-2 challenge (Ullah et al., 2021a). Similarly, two other studies examining humoral responses in acutely infected individuals found that Fc-mediated effector functions were associated with survival (Brunet-Ratnasingham et al., 2021; Zohar et al., 2020). Therefore, while antibody-mediated neutralization was required for protection, it was not sufficient for viral control.

Serological analysis of the plasma or serum from SARS-CoV-2-infected individuals from multiple sources (Harvey et al., 2021; McCallum et al., 2021; Piccoli et al., 2020) revealed that ~65%–80% of the neutralizing response was from RBD-specific antibodies, with a smaller portion targeting the NTD (~6%–20%) or the S2 subunit (4%–20%). Despite the limited immunogenicity of the glycan-shielded NTD, NTD-directed antibodies also impose selection pressure to elicit NTD escape mutations and deletions in emerging SARS-CoV-2 variants (McCallum et al., 2021). Notably, NTD-directed monoclonal nAbs whose structures have been determined recognized a similar glycan-free epitope (Cerutti et al., 2021; Chi et al., 2020; Liu et al., 2020; McCallum et al., 2021; Sun et al., 2021; Voss et al., 2021), named the NTD supersite (residues 14–20, 140–158, and 245–264) (Harvey et al., 2021; McCallum et al., 2021). The higher number of mutations within the NTD supersite than the NTD scaffold highlights its importance to the virus (McCarthy et al., 2021). Given that the NTD-supersite-directed nAbs do not interfere with the ACE2-RBD interaction or the shedding of the S1 subunit, their mechanism of neutralization is yet to be determined.

Here, we sought to test if Fc-mediated effector functions of antibodies alone could mediate virological control in a lethal K18-hACE2 transgenic mouse model of SARS-CoV-2 using CV3-13, a non-neutralizing antibody (non-nAb) with potent Fc-effector functions. Our cryoelectron microscopy (cryo-EM) structure revealed that CV3-13 binds to an NTD epitope that partially overlaps with the NTD supersite with a distinct angle of approach, adding to our understanding of how fine epitope specificity and the mode of antibody binding can contribute to antibody function. Several recurrent NTD mutations outside of the NTD supersite associated with immune resistance are found within the CV3-13 epitope, e.g., the N2 loop and the identified N2-3 hairpin, suggesting that the epitope coincides with those of other NTD-binding antibodies. While administration of CV3-13 under both prophylactic and therapeutic regimens did not change the replication dynamics of SARS-CoV-2 in K18-hACE2 mouse model, an Fc-enhanced version of CV3-13 significantly delayed virus spread, neuroinvasion, and death under prophylactic settings. Remarkably, Fc-enhanced CV3-13 synergistically protected mice from lethal SARS-CoV-2 infection when combined with Fc-compromised neutralizing anti-S2 antibody CV3-25. Thus, using an NTD-binding non-nAb, we demonstrate the impact of Fc-effector functions in mitigating virus-induced pathogenesis and spread as well as its contribution toward enhancing overall *in vivo* efficacy in antibody cocktails.

RESULTS

CV3-13 binds the NTD of the spike glycoprotein

To test if non-nAbs alone can protect from SARS-CoV-2 infection, we characterized a non-nAb isolated from the peripheral blood mononuclear cells (PBMCs) of a convalescent individual (CV3) 6 weeks after the onset of symptoms. Using fluorescent SARS-CoV-2 spike 2P as a probe, we sorted 432 antigen-specific B cells from this donor PBMCs. We successfully generated 27 monoclonal antibodies and tested their ability to neutralize pseudoviral particles carrying the spike. CV3-13 bound to the spike but did not neutralize SARS-CoV-2 pseudovirus (Jennewein et al., 2021). To determine the epitope recognized by CV3-13, we analyzed its ability to bind different spike variants on the surface of transfected cells. CV3-13 efficiently bound the WT (Wuhan-Hu-1 reference strain) and the D614G variant but did not recognize the spike from the B.1.1.7 (alpha) variant (Figures 1A and 1B). We took advantage of this differential binding capacity to determine the epitope of CV3-13 by sequentially introducing B.1.1.7 variant mutations into the WT spike. CV3-13 recognized all but the Δ144 mutant that had a single amino acid deletion located in the S1 NTD (Figure 1B). In agreement with our cell surface binding data, surface plasmon resonance showed that CV3-13 binds to the SARS-CoV-2 S1 subunit (Figure 1C). Monovalent CV3-13 Fab bound to the stabilized spike trimer ectodomain (spike-6P) with nanomolar affinity (K_D = ~55 nM) (Figure 1D).

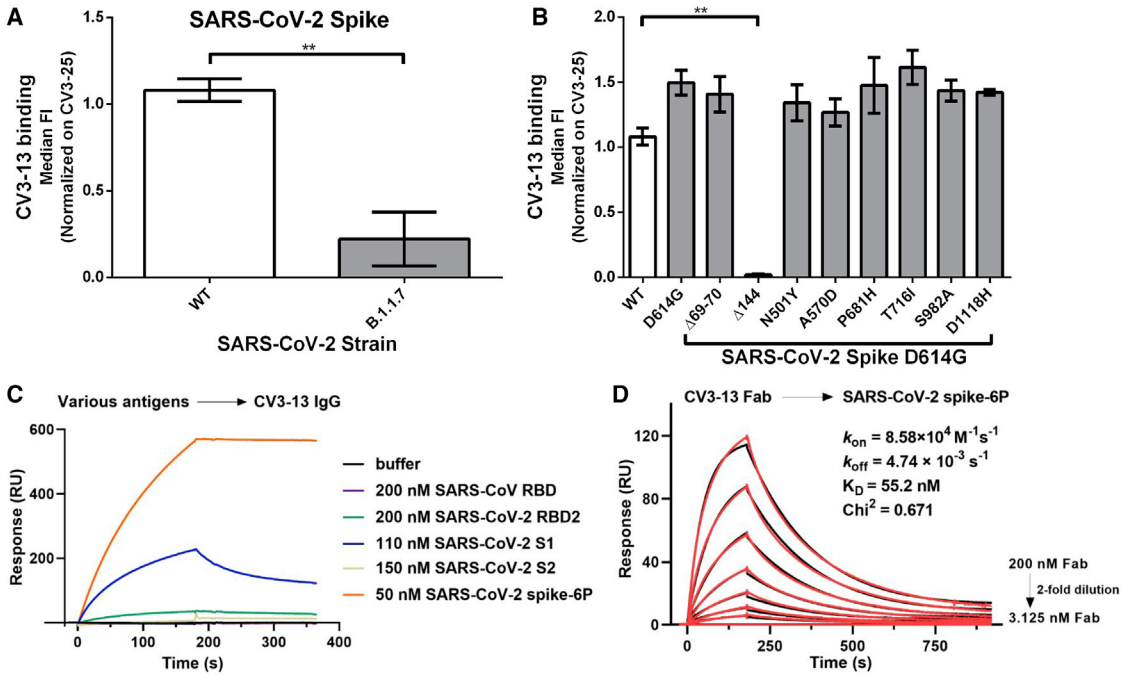

Figure 1. Recognition of SARS-CoV-2 spikes by CV3-13

(A) Staining of CV3-13 (5 μg/mL) on the spike of the WT (Wuhan-Hu-1) or the B.1.1.7 (alpha variant) strain of SARS-CoV-2 expressed at the surface of 293T-transfected cells.

(B) Staining of CV3-13 (5 μg/mL) on the different individual mutations of the spike of the B.1.1.7 strain of SARS-CoV-2 (D614G, Δ69-70, Δ144, N501Y, A570D, P681H, T716I, S982A, and D1118H). CV3-13 binding was further normalized to the binding obtained with the conformational-independent CV3-25 mAb (5 μg/mL). Statistical significance was evaluated using a non-parametric Mann-Whitney U test (**$p < 0.01$). Data are the average of the median of each experiment done at least two times. Mean values ± standard error of the mean (SEM).

(C) Surface plasmon resonance-based epitope mapping reveals that CV3-13 explicitly binds to SARS-CoV-2 spike S1 subunit. Different viral antigens from SARS-CoV or SARS-CoV-2 were injected to the immobilized CV3-13 IgG (~5,800 RU) at the indicated concentrations.

(D) Kinetics measurement of CV3-13 Fab binding to the immobilized SARS-CoV-2 HexaPro spike (~800 RU) with concentrations ranging from 3.125 to 200 nM (2-fold serial dilution). The experimental data (red) were fitted to a 1:1 Langmuir model (black) in BIA evaluation software.

CV3-13 is a non-nAb with potent Fc-mediated effector functions

To confirm that CV3-13 was a non-nAb (Jennewein et al., 2021), we tested its capacity to neutralize pseudoviruses carrying the SARS-CoV-2 spike. For comparison purposes, we used CV3-1, a potent RBD-targeting nAb, as a positive control (Jennewein et al., 2021). CV3-1 was recently shown to protect K18-hACE2 mice from a lethal SARS-CoV-2 challenge in an Fc-effector function-dependent manner (Ullah et al., 2021a). Our analyses showed that CV3-13 was unable to neutralize pseudoviral particles (Figure 2A) bearing the SARS-CoV-2 spike or the live virus (Figure 2B). Introduction of LALA or GASDALIE mutations to the Fc portion of the antibody did not modify its neutralization profile (Figures 2A and 2B) or its ability to recognize the spike whether it be at the surface of infected cells, transduced cells, transfected cells, or the recombinant SARS-CoV-2 S-6P (Figures 2C, 2D, 2G, and 2H). The LALA (L234A/L235A) mutations impair the interaction between the IgG Fc portion and FcγRs (Saunders, 2019), while GASDALIE (G236A/S239D/A330L/I332E) mutations strengthen these interactions (Bournazos et al., 2014; DiLillo and Ravetch, 2015; Lazar et al., 2006; Richards et al., 2008; Smith et al., 2012). Having established that CV3-13 does not mediate neutralization (Figures 2A and 2B), we then evaluated whether it could mediate Fc-effector functions. To this end we used an ADCC assay using a human T lymphoid cell line resistant to non-specific NK cell-mediated cell lysis (CEM.NKr) and stably expressing the full-length spike on their surface as target cells. PBMCs from healthy individuals were used as effector cells, as previously reported (Anand et al., 2021; Beaudoin-Bussieres et al., 2021). In agreement with a previous study, CV3-1 mediated robust ADCC (Ullah et al., 2021a) (Figure 2E). CV3-13 mediated ADCC to a similar level than CV3-1 (Figure 2E). Introduction of the GASDALIE mutations enhanced CV3-13-mediated ADCC to levels surpassing those achieved with CV3-1 or CV3-13 WT at higher concentrations (Figure 2E). As expected, introduction of the LALA mutations significantly decreased CV3-13-mediated ADCC (Figure 2E). CV3-13 GASDALIE mediated similar ADCP as its WT counterpart, while CV3-13 LALA mediated reduced ADCP (at all tested concentrations) compared with both CV3-13 WT and CV3-13 GASDALIE (Figure 2F). Altogether, these results confirm that CV3-13 is a non-nAb able to mediate Fc-effector functions.

Structural analyses of the CV3-13 Fab and SARS-CoV-2 spike complex defines an NTD epitope

To define the CV3-13 epitope and gain a more comprehensive understanding of how CV3-13 triggers potent Fc-mediated

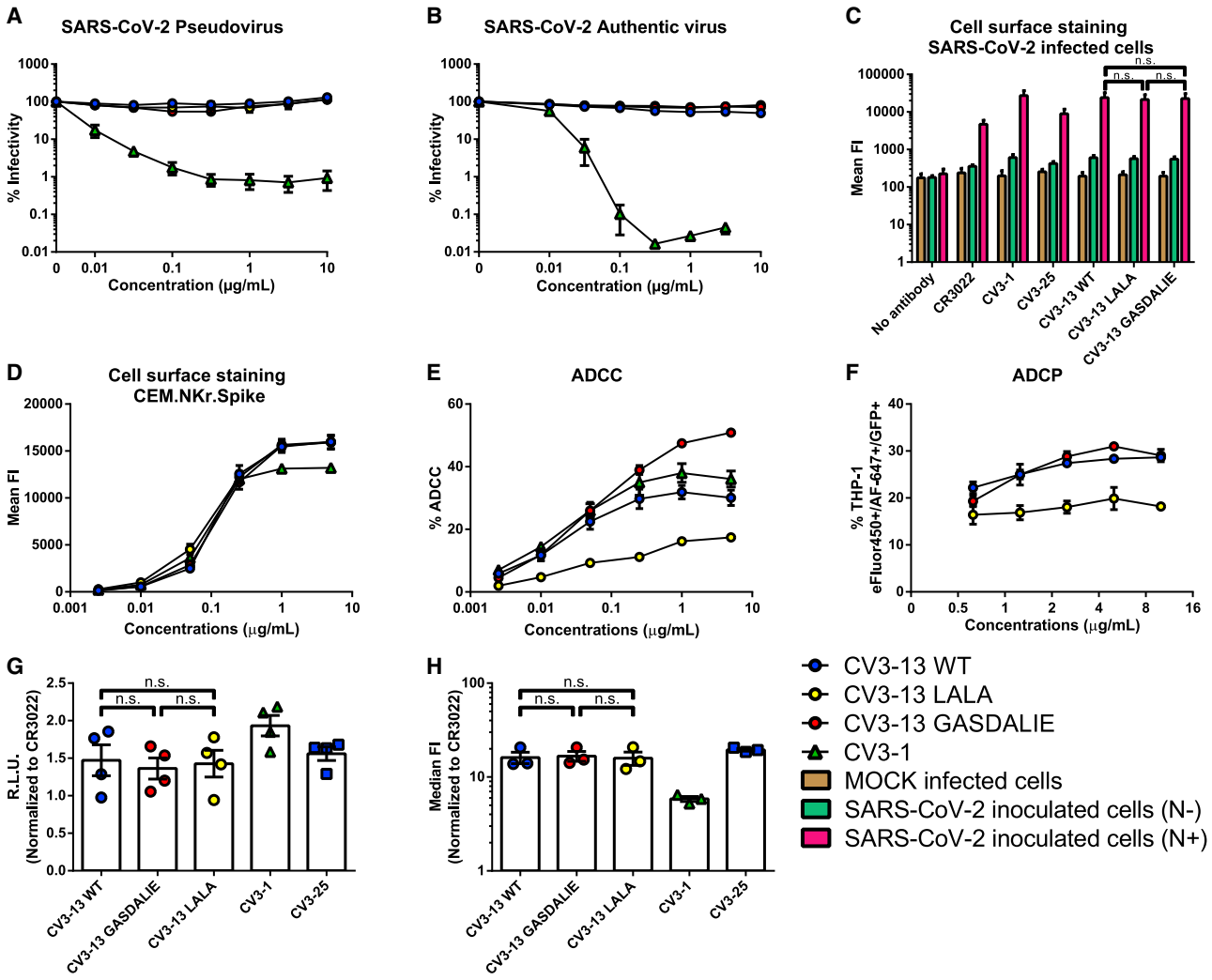

Figure 2. CV3-13 is a non-nAb that has potent Fc-mediated effector functions

(A) Neutralizing activity of CV3-13 WT, CV3-13 LALA, CV3-13 GASDALIE, and CV3-1 on SARS-CoV-2 spike D614G bearing pseudoviruses using 293T-ACE2 target cells.

(B) Neutralizing activity of CV3-13 WT, CV3-13 LALA, CV3-13 GASDALIE, and CV3-1 on SARS-CoV-2 D614G authentic virus using Vero E6 target cells. The concentrations are the same as in (A).

(C) Binding of CR3022, CV3-1, CV3-25, CV3-13 WT, CV3-13 GASDALIE, and CV3-13 LALA on the surface of Vero E6 cells infected with authentic SARS-CoV-2 virus 48 h post infection. Intracellular nucleocapsid (N) staining was done to separate the infected from the uninfected cells.

(D) Binding of CV3-13 WT, CV3-13 LALA, CV3-13 GASDALIE. and CV3-1 on CEM.NKr.Spike cells. The non-specific staining obtained of CEM.NKr parental cells was subtracted from the staining on CEM.NKr.Spike cells.

(E) % ADCC in the presence of CV3-13 WT, CV3-13 LALA, CV3-13 GASDALIE, and CV3-1 using a 1:1 ratio of parental CEM.NKr cells and CEM.NKr.Spike cells as target cells while PBMCs from uninfected donors were used as effector cells.

(F) Percent ADCP mediated by CV3-13 WT, CV3-13 LALA and CV3-13 GASDALIE using CEM.NKr.Spike cells as target cells and THP-1 cells as phagocytic cells.

(G) Indirect ELISA on SARS-CoV-2 spike 6P using CV3-13 WT, CV3-13 LALA, CV3-13 GASDALIE, CV3-1, CV3-25, and CR3022 (50 ng/mL). CR3022 was used as a positive control in each ELISA plate and for each experiment the data were further normalized on the signal obtained with this antibody. Data shown is the average of four independent experiments.

(H) Staining with CV3-13 WT, CV3-13 LALA, CV3-13 GASDALIE, CV3-1, CV3-25, and CR3022 (5 µg/mL) of 293T cells transfected with the SARS-CoV-2 spike. CR3022 was used as a positive control in each experiment and for each experiment the data were further normalized on the signal obtained with this antibody. Data shown are the average of three independent experiments. Statistical significance was evaluated using a non-parametric Mann-Whitney U test (n.s., not significant). Mean FI, mean fluorescence intensity; Median FI, median fluorescence intensity; R.L.U., relative light units. The error bars indicate the SEM. Data are the average of at least two experiments for (A–F).

cytotoxicity without directly neutralizing the SARS-CoV-2 virus, we determined the cryo-EM structure of the SARS-CoV-2 HexaPro spike in complex with CV3-13 Fab at a resolution of 4.45 Å (FSC cutoff 0.143) using C1 symmetry (Figures 3 and S1). The spike trimer presented itself in the one-RBD-up conformation with each of the NTD bound to one CV3-13 Fab to the furthest lateral side of the spike relative to the spike trimer axis. Despite the asymmetric RBD conformation in the three spike protomers, the three CV3-13-NTD interfaces were identical. Global refinement imposed with C3 symmetry improved the overall resolution to 4.19 Å and permitted a detailed analysis of the CV3-13 footprint. The C3 symmetry map was therefore used in all further structural analysis (Figures 3 and S1).

The structure of CV3-13 Fab bound to the SARS-CoV-2 HexaPro spike is shown in Figure 3A. The variable heavy and light chain regions (V_H and V_L) of CV3-13 were well defined in the density. The constant part of the Fab was disordered, however, and is omitted from the model. CV3-13 binds to the NTD at an almost right angle relative to the stem region of the spike. Both heavy and light chain complementarity determining regions (CDRs) of CV3-13 contribute almost equally to antigen recognition with CDR H3, CDR L1, and CDR L3 presenting most contacts. The total buried surface area (BSA) in complex formation is 1184 $Å^2$, which is comparable with the BSA of typical complexes formed by other NTD-specific antibodies (Figure 3B). Four out of five highly mobile NTD loops as defined by Chi et al. (2020), e.g., N2 (residues 67–79), N3 (residues 141–156), N4 (residues 177–186), and N5 (residues 246–260) are stabilized by the associated CV3-13 Fab (Figure 3C). The fifth antigenic NTD loop N1 (residues 14–26) is distal from the CV3-13 binding site and exhibits a higher degree of mobility in the complex. Of the antibody CDRs, the 14-amino-acid CDR H3, consisting of 7 aromatic residues (6 tyrosines and 1 phenylalanine), stretches into the hydrophilic groove formed by the positively charged N3 and N4 loops, the N2 and N3 loops, and the glycan-shielded Asn^{122}. CV3-13 forms extensive contact with N2, N4, and a buried N2-3 hairpin (residues 95–102), which are rarely involved in the epitopes of other known NTD mAbs (Figure 4C). Interestingly, CV3-13 relies on key π-π interactions through its CDR H3 tyrosines to the Tyr^{144}-Tyr^{145} stretch of N3 that is frequently mutated in SARS-CoV-2 emerging variants. For example, the single residue deletion of Tyr^{144} (as first detected in the B.1.1.7 variant), which was used to initially characterize CV3-13, causes a complete abrogation of CV3-13 binding (Figure 1B).

The footprint of the CV3-13 epitope differs from all known nAbs that recognize the NTD. Neutralizing NTD-directed antibodies target similar glycan-free epitopes located in the upper protruding area of the NTD, referred to as the "NTD supersite" of vulnerability (Cerutti et al., 2021; Harvey et al., 2021; McCallum et al., 2021). The non-nAb CV3-13 targets a distinct lateral region of the spike closer to the viral membrane surface, which only marginally overlaps with the supersite (Figure 4A). The distinct angle of approach of CV3-13 enables its extended CDR H3 to access the buried N2-3 hairpin, which does not interact with the reported NTD-directed mAbs. Given that the NTD mutations found in escape variants of SARS-CoV-2 are thought to be the direct result of NTD-specific antibody selection, the emergence of the T95I mutation in the N2-3 hairpin, as seen in the B.1.526 (iota) and B.1.617.1 (kappa) variants (Figure S2), suggests that this region represents an antigenic site that can be targeted by non-nAb antibodies. Interestingly, the immunogenic N3 and N5 loops, which form the major interacting motifs for currently characterized NTD mAbs, and is the primary component of the NTD supersite, only makes minor contact with the CDR H3, and L1 and L2 of CV3-13. As a result, the backbone residues of the N3 and N5 loops are less traceable in the density map (Figure S3) and appear to adopt markedly different conformations as compared with those observed for neutralizing anti-NTD mAb structures (Figure 4E). Overall, the N3 and N5 loops, which form the majority of the NTD supersite are less important for CV3-13 binding. Instead, CV3-13 utilizes the N2 and N4 loops and N2-3 hairpin, which are located at the lateral/bottom side of the NTD and are rarely accessed by the NTD-directed nAbs that bind from the top of the NTD. Our data are consistent with the finding that N3 and N5 loop engagement is an important component of NTD-directed antibody neutralization of SARS-CoV-2.

CV3-13 has a distinct angle of approach and induces conformational rearrangements in the NTD as compared with other NTD-binding mAbs

To gain structural insight on how the antibody recognition site and its angle of approach to the SARS-CoV-2 spike NTD affects the mode of action (i.e., potent neutralizers targeting the supersite versus non-nAb), we aligned the NTD-Fv portions of CV3-13 and other reported NTD-directed antibodies based on the rigid NTD core. The comparisons consisted of antigen-Fab structures for whose Protein Data Bank (PDB) models are available, including 11 neutralizing antibodies targeting the NTD supersite as well as the other three which recognize the so-called infectivity-enhancing site (Li et al., 2021a; Liu et al., 2021; McCallum et al., 2021). As shown in Figure 4A, CV3-13 approaches the NTD at a nearly perpendicular angle relative to the spike trimer axis with its epitope footprint only partly overlapping the NTD supersite and the infectivity-enhancing site. The supersite-binding antibodies access the NTD from the top of the spike trimer, while antibodies targeting the infectivity-enhancing site approach the spike from the bottom, closer to the viral membrane. The differences in binding modes of CV3-13 and other NTD-specific antibodies are evident when the angles of approach (defined as the angle between the average Cα position for the Fv of each individual mAb [$Cα\text{-}_{Fv}$], and the average Cα position for the NTD as a whole [Cα-NTD], using the average Cα position of the C-terminal helix [residues 295–303] of the NTD [Cα-NTD-C-term] as the origin to exclude any differences due to the conformational state of the NTD relative to the spike as a whole) are calculated (Figure 4B). The supersite-binding nAbs approach the NTD with a similar angle (in a range of 6°–15°), substantially different from that of CV3-13s with a calculated angle of ~30° (Figure 4B). In contrast, the infectivity-enhancing antibodies use the angle of approach in the range of 45°–60°. Also, the fine epitope specificity of CV3-13 is different with contact regions only partially overlapping with the neutralization supersite (Figure 4C). To summarize, CV3-13 uses the binding angle that positions it somewhere between the binding angles of antibodies recognizing the neutralization supersite, that bind from the top of the spike and

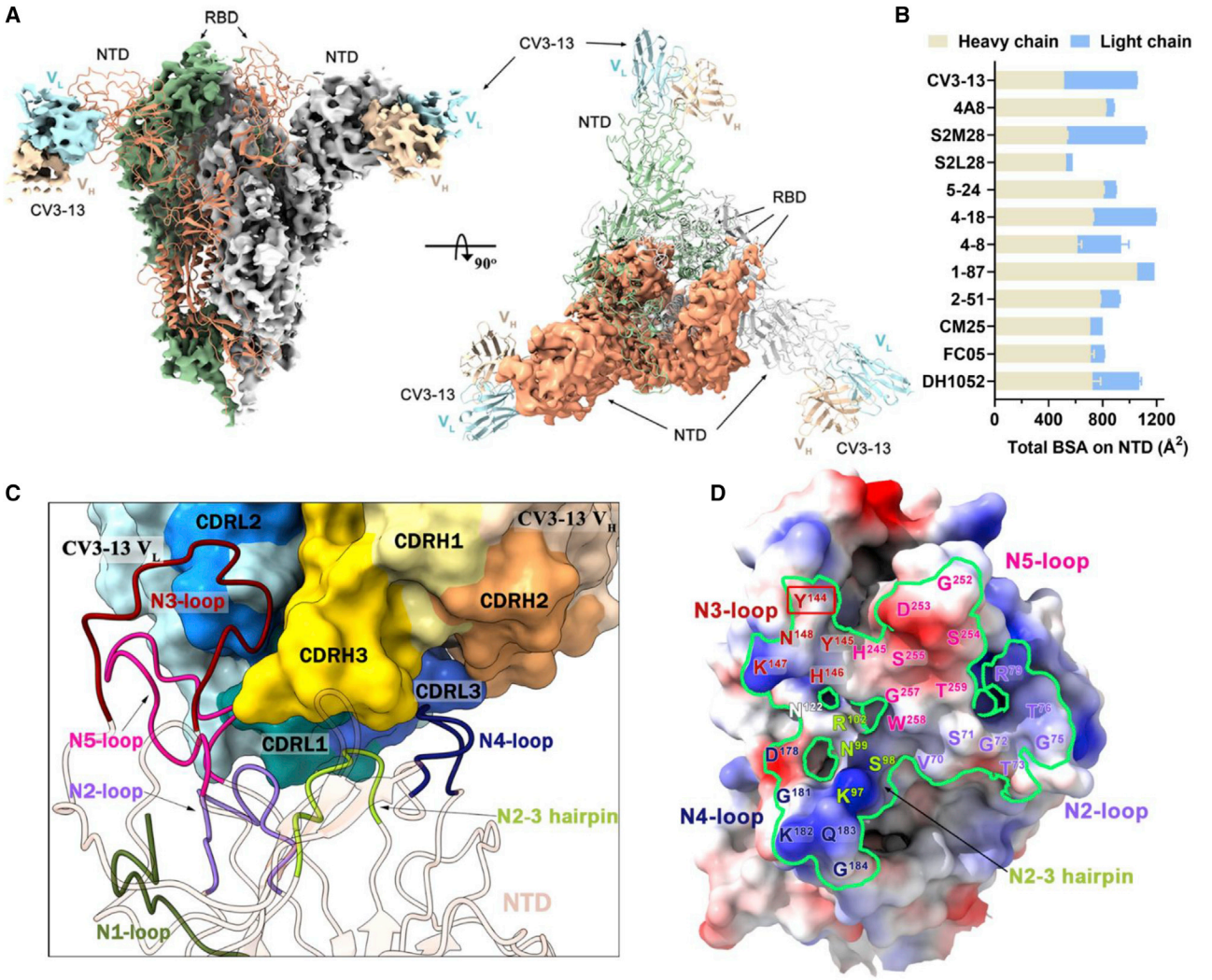

Figure 3. Cryo-EM structure of SARS-CoV-2 spike in complex with CV3-13 Fab

(A) Side and top views of the NTD-targeting CV3-13 Fab and SARS-CoV-2 spike complex reveal a symmetrical Fab-spike assembly. In the left panel, protomer A of the spike colored in salmon is shown in ribbons while the other two protomers colored in green or gray and the variable regions (heavy chain, light yellow; light chain, cyan) of three CV3-13 Fabs binding to the lateral surface of the NTD are shown as cryo-EM density (C3 symmetry map).

(B) The total buried surface area (BSA) at the Fab/NTD interface contributed by heavy/light chains of CV3-13 and 11 other structurally available NTD-directed mAbs, 4A8 (PDB: 7CL2), S2M28 (PDB: 7LY3), S2L28 (PDB: 7LXX), 5–24 (PDB: 7L2F), 4–18 (PDB: 7L2E), 4–8 (PDB: 7LQV), 1–87 (PDB: 7L2D), 2–51 (PDB: 7L2C), CM25 (PDB: 7M8J), FC05 (PDB: 7CWS), and DH1052 (PDB: 7LAB). The BSA values of all the equivalent biological assemblies were calculated and averaged by PISA (Krissinel and Henrick, 2007).

(C) Expanded view of CV3-13 interactions with the protruding NTD loops. CV3-13 is shown as surface with the CDRs H1, H2, H3 L1, L2, and L3 colored in yellow, orange, gold, dark cyan, sky blue, and deep blue, respectively. The NTD regions are displayed as ribbons and the N1 to N5 loops as defined by Chi et al. (2020) are colored in green, purple, deep red, blue, and pink, respectively. Of note, the identified N2-3 hairpin is highlighted in light green.

(D) CV3-13 epitope footprint on the electrostatic potential surface of NTD (colored red, blue, and white for negative, positive, and neutral electrostatic potential, respectively). The NTD residues interacting with CV3-13, which were defined as those with BSA > 0 Å^2 as calculated by PISA, are colored as in (C) in accordance with loop locations. The CV3-13 epitope footprints are outlined in green. The deleted Y^{144} identified in the B.1.1.7 variant that disrupts CV3-13 binding is marked with a red box.

antibodies targeting the infectivity-enhancing site, that bind at the bottom of the spike, closer to the viral membrane. These features are likely why CV3-13 lacks direct neutralizing activity but has no infectivity-enhancing properties (Figures 2A, 2B, and S4C). The CV3-13 binding mode permits effective engagement of innate immune cells to mediate Fc-effector activity. Indeed, it has been shown that antibodies targeting the NTD supersite have largely overlapping epitope footprints (all engaging the N1, N3, and N5 NTD loops) and a narrow range in their angle of approach that could allow them to sterically disrupt spike-receptor interactions, TMPRSS2-dependent activation and/or viral-host membrane fusion.

Both CV3-13 and the supersite-specific nAbs bind to the NTD via a set of highly mobile NTD loops. To assess the impact of

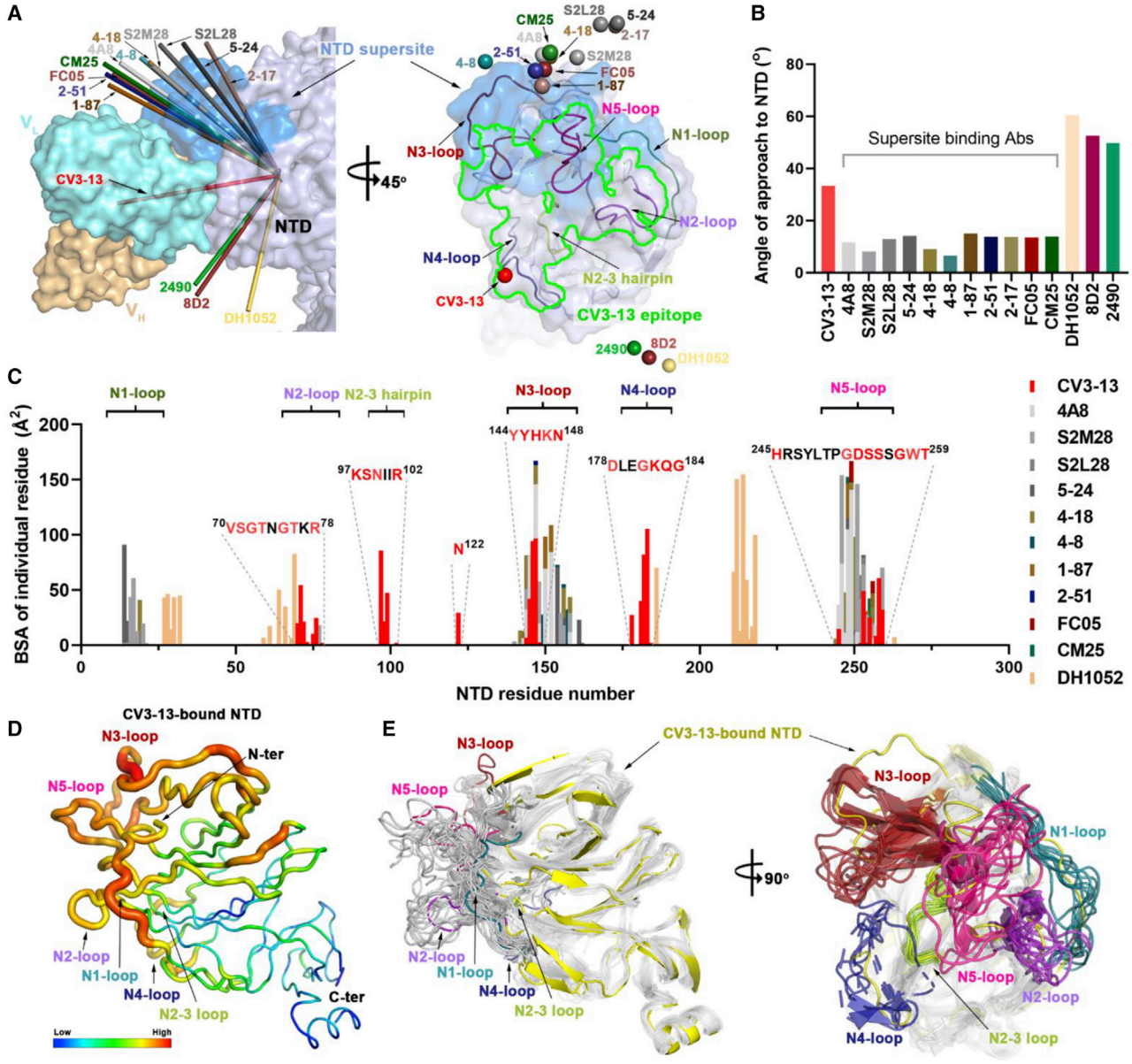

Figure 4. Structural basis of SARS-CoV-2 spike recognition by CV3-13 and NTD-directed nAbs

(A) Two-view diagram of CV3-13 binding to the NTD lateral epitope as compared with 11 other NTD-targeting neutralizing mAbs and 3 other infectivity-enhancing mAbs. The NTD defined in this study is used here and shown as a light blue surface with the NTD supersite (residues 14–20, 140–158, and 245–264) highlighted in blue. On the left panel, the CV3-13 variable region is shown as a surface in light yellow for heavy chains and cyan for light chains. The approach of other NTD-binding mAbs are graphically represented by arrows (using the average Cα position of the variable region for individual NTD-targeting antibodies [$C\alpha\text{-}_{Fv}$] pointing toward the average Cα position of the NTD domains as a whole [$C\alpha\text{-}_{NTD}$] determined by individual NTD/spike-mAb complexes) in the indicated colors. On the right panel, the NTD is shown in a semi-transparent surface with NTD loops N1-N5 and the defined N2-3 hairpin shown as colored ribbons. The CV3-13 epitope boundary is shown with a green line. The $C\alpha\text{-}_{Fv}$ of each NTD antibody is shown as colored spheres.

(B) Angles of approach of CV3-13 and other NTD antibodies. The values for individual mAbs are calculated as the angle between $C\alpha\text{-}_{Fv}$ and $C\alpha\text{-}_{NTD}$, with $C\alpha\text{-}_{NTD\text{-}Cter}$ acting as the origin.

(C) Diagram of NTD antibody epitopes reveal a distinct set of CV3-13 interacting NTD residues. The buried surface area (BSA) for the NTD residues contacting individual mAbs were calculated by PISA.

(D) B factor representation of the CV3-13-bound NTD domain.

(E) Orthogonal views of the NTD superimposition of reported EM/X-ray structures of NTD-binding mAbs in complex with SARS-CoV-2 spike or NTD. On the left panel, N1-N5 loops and the N2-3 hairpin of CV3-13-bound NTD are shown as colored ribbons with the NTD scaffold colored in yellow, while the other NTDs are uniformly depicted as gray ribbons. In the right panel, CV3-13-bound NTD is shown by yellow ribbons and the antigen NTD loops from other mAb-NTD structures are shown with colored ribbons with the scaffold colored in gray.

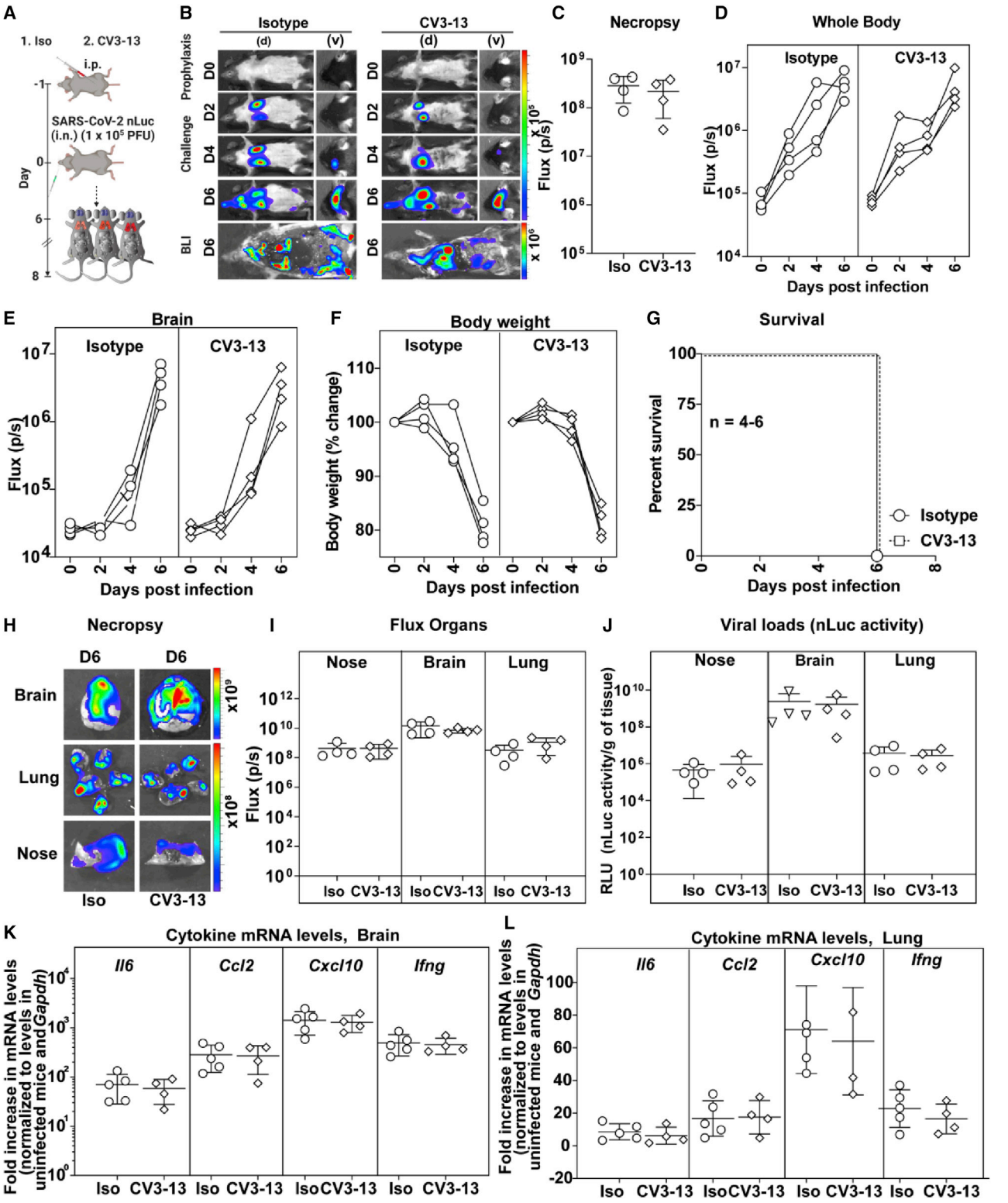

Figure 5. Prophylactic treatment with non-nAb CV3-13 does not protect K18-hACE2 mice from lethal SARS-CoV-2 infection

(A) Experimental design for testing *in vivo* efficacy of non-nAb CV3-13 administered 1 day before challenging K18-hACE2 mice (i.n.) with SARS-CoV-2-nLuc followed by non-invasive BLI every 2 days. Human IgG1-treated (12.5 mg IgG/kg) mice were use as the isotype control (Iso).

(legend continued on next page)

antibody recognition on the conformation of NTD, we superimposed the NTD domain from the ligand-free HexaPro spike (PDB: 6XKL) and 11 NTD-directed antibody-spike/NTD complexes and examined mAb-induced structural rearrangements. As described earlier by Cerutti et al. (2021), the highly mobile N1-N5 loops (Figure 4D), which are largely disordered in the ligand-free spike, have diverse conformations in response to the bound Fabs at different sites (Figure 4E). The degree of local flexibility for the NTD loops is inversely correlated with their contribution to the Fab-NTD interface. These substantial structural rearrangement of the NTD are a direct consequence of antibody binding, either by a conformational sampling or an induced-fit mechanism. Collectively, the high immunogenicity and high mutational frequency observed in the flexible NTD loops are likely associated with their increased accessibility to both neutralizing and non-nAbs.

CV3-13 does not protect K18-hACE2 mice from a SARS-CoV-2 lethal challenge

We next investigated the *in vivo* efficacy of the non-nAb CV3-13 under a prophylactic (24 h prior) or therapeutic (1 and 2 days post infection [dpi]) setting to protect or treat K18-hACE2 mice from a lethal intranasal SARS-CoV-2 nLuc infection as described previously (Figures 5A and S5A) (Ullah et al., 2021a). Longitudinal non-invasive bioluminescence imaging (BLI), body weight change, survival, viral load estimation in brain, lung, and nasal cavity, and terminal imaging after necropsy showed no difference between isotype- and CV3-13-treated mice under either prophylactic or therapeutic settings (Figures 5 and S5B–S5J). Furthermore, mRNA levels of inflammatory cytokines (*IL6*, *CCL2*, *CXCL10*, and *IFNG*) in brain and lungs were also similar to isotype-treated cohorts (Figures 5, S5K, and S5L). These data suggest that natural Fc-effector functions associated with CV3-13 were not enough to alter virus replication and dissemination *in vivo* in the stringent K18-hACE2 mouse model of SARS-CoV-2 infection. Thus, in addition to clearing infected cells by engaging innate immune cells through Fc-mediated effector functions, efficient Fab-mediated neutralization of free viruses by antibodies is essential for optimal *in vivo* efficacy.

CV3-13 GASDALIE prophylaxis decreases SARS-CoV-2 spread and neuroinvasion in K18-hACE2 mice

Non-nAbs inactivate free viruses or clear infected cells predominantly by engaging innate immune components through the Fc region. We therefore explored if Fc-effector function-enhancing mutations (GASDALIE) could improve the *in vivo* efficacy of CV3-13 against SARS-CoV-2 in a prophylactic setting. Since human IgGs bind to mouse FcγRs with similar affinity as human IgGs on human FcγRs (Dekkers et al., 2017) GASDALIE mutations which increase binding on human FcγR at the surface of effector cells are also expected to increase the binding to mouse FcγRs. We first confirmed that the GASDALIE mutations significantly enhanced Fc-mediated effector functions of CV3-13 without altering its non-nAb phenotype (Figures 2A, 2B, 2E, S4B, and S4C). Next, we carried out temporal BLI to compare SARS-CoV-2-nLuc dissemination in K18-hACE2 mice that were pre-treated with CV3-13 WT and CV3-13 GASDALIE (Figure 6A). Whole-body quantification of nLuc signal intensities both non-invasively and after necropsy at 4 dpi revealed significant reduction in SARS-CoV-2 replication and neuroinvasion in CV3-13 GASDALIE-pre-treated mice compared with isotype and CV3-13 WT pre-treated cohorts (Figures 6B–6E). In addition, immunostaining of brain cryosections with antibodies to the SARS-CoV-2 nucleocapsid revealed a marked reduction in infected cells when mice were pre-treated with CV3-13 GASDALIE (Figures S6A and S6B). Both CV3-13 WT and CV3-13 GASDALIE mAbs decorated the surface of infected neurons suggesting that introduction of GASDALIE mutations did not hamper antibody penetration into tissue despite enhanced FcγR interactions (Figure S6B). We also observed a significant difference in body weight loss phenotype and an overall decrease in systemic spread of virus to most tissue analyzed except lungs after necropsy as measured by nLuc flux intensities and viral load analyses by real-time PCR for N mRNA copy numbers (Figures 6F–6H and S6C). While viral loads and cytokine mRNA in the lungs were similar between the cohorts, there was a significant decrease in the overall inflammatory cytokine mRNA levels in the brain consistent with reduced viral loads in CV3-13 GASDALIE-treated mice (Figure 6I–6K). Thus, our data indicate that prophylaxis with CV3-13 GASDALIE significantly decreases SARS-CoV-2 dissemination and neuroinvasion in mice.

CV3-13 GASDALIE prophylaxis delays mortality and protects mice from lethal SARS-CoV-2 challenge when combined with Fc-compromised nAb CV3-25

To test if CV3-13 GASDALIE-imposed reduction in virus dissemination had any impact on SARS-CoV-2-induced mortality in K18-hACE2 mice, we extended our experimental endpoint to assess survival (Figure 7A). In addition to hIgG1-pre-treated cohort, we also included mice treated with an unrelated antibody

(B) Representative images from BLI of SARS-CoV-2-nLuc-infected mice in ventral (v) and dorsal (d) positions at the indicated dpi and after necropsy for experiment as in (A).
(C) *Ex vivo* quantification of the nLuc signal as flux (photons/sec) after necropsy.
(D and E) Temporal quantification of the nLuc signal as flux (photons/s) computed non-invasively in indicated areas of each animal.
(F) Temporal changes in mouse body weight with initial body weight set to 100%.
(G) Kaplan-Meier survival curves of mice statistically compared by log rank (Mantel-Cox) test for experiment as in (A).
(H and I) *Ex vivo* imaging of organs and quantification of the nLuc signal as flux (photons/s) at the indicated dpi after necropsy.
(J) Viral loads (nLuc activity/g) from the indicated organs using Vero E6 cells as targets.
(K and L) Cytokine mRNA levels in lung and brain tissues after necropsy normalized to *Gapdh* in the same sample and that in uninfected mice. Viral loads (J) and inflammatory cytokine profile (K and L) were determined after necropsy for mice that succumbed to infection. Scale bars in (B) and (H) denote radiance (photons/s/cm^2/steradian). Each curve in (D–F) and each data point in (C) and (I–L) represents an individual mouse. An equal number of female and male mice were used in each group. The data in (C) and (I–L) were analyzed by non-parametric Mann-Whitney test. Comparisons shown as "n.s." or lacking * indicate non-significant statistical significance $p > 0.05$, Mean values ± SD are depicted.

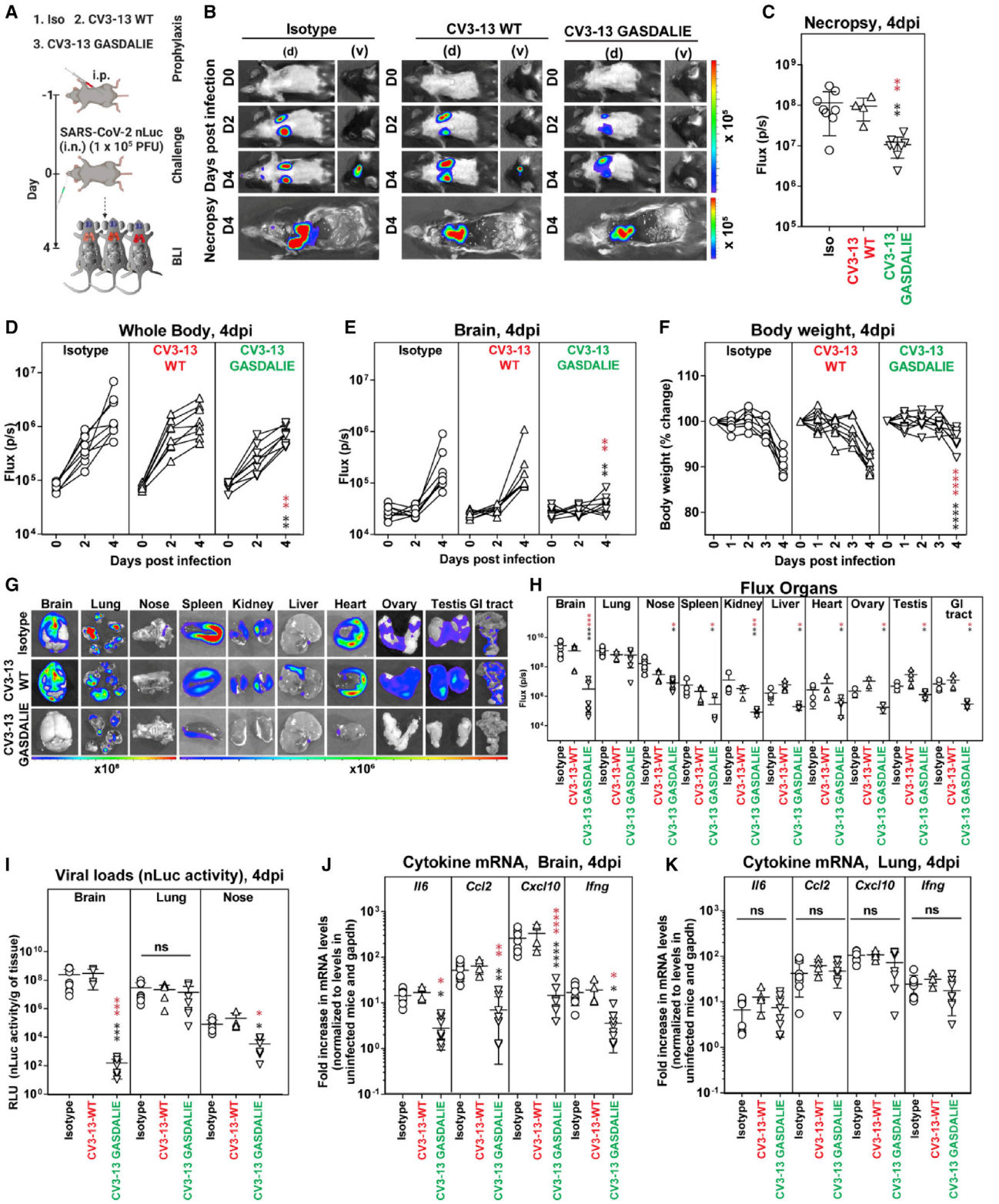

Figure 6. Prophylactic treatment with CV3-13 GASDALIE delays SARS-CoV-2 neuroinvasion and dissemination in K18-hACE2 mice

(A) Experimental design for testing virus dissemination in CV3-13 WT and CV3-13 GASDALIE-administered K18-hACE2 mice, 1 day before challenging (i.n.) with SARS-CoV-2-nLuc followed by non-invasive BLI every 2 days. Human IgG1-treated (12.5 mg IgG/kg) mice were use as the isotype control.

(legend continued on next page)

that recognizes the HIV-1 co-receptor binding site on gp120 (17b) carrying GASDALIE mutations as controls. In corroboration with early termination (4 dpi) experiment, our BLI analyses revealed a significant delay in systemic virus spread as well as neuroinvasion in CV3-13 GASDALIE-administered mice compared with control and CV3-13 WT-pre-treated cohorts (Figures 7B–7D). Accordingly, we also observed a significant deceleration in body weight loss and mortality for CV3-13 GASDALIE-pre-treated mice (Figures 7E and 7F). In addition, viral loads in nose, brain, and lungs were significantly reduced in the CV3-13 GASDALIE-pre-treated group compared with the CV3-13-pre-treated and control cohorts (Figures 7G and 7H). In contrast to 4 dpi, where viral loads in the lungs were comparable with control cohorts, we did observe a significant reduction of viral loads in the lungs of CV3-13 GASDALIE-pre-treated mice after they had succumbed to infection (Figure 7H). These data indicated that CV3-13 GASDALIE required additional time to reduce virus infection in the lungs. However, inflammatory cytokine mRNA expression profile in the lungs remained comparable in CV3-13 GASDALIE-treated mice with significant reduction seen only for *Ccl2* and *Ifng* mRNA levels in the brain tissues as compared with control cohorts. These data demonstrate the potential of non-nAbs with enhanced Fc-effector functions to interfere with SARS-CoV-2 spread.

We next explored if *in vivo* efficacy can be improved when Fc-enhanced CV3-13 is combined with a nAb. We chose a nAb CV3-25 that binds S2 for the analyses with Fc-compromising LALA mutations. Combining nAb CV3-25 LALA with non-nAb CV3-13 GASDALIE also allowed us to separate neutralizing and Fc-effector functions of antibodies for gaining mechanistic insights into antibody action. Introduction of the GASDALIE and the LALA mutations in CV3-13 and CV3-25, respectively, did not modify their capacity to bind to the spike or change their neutralizing profile compared with their WT counterparts (Figures S4A and S4C). As predicted, these Fc changes affected their capacity to mediate ADCC (i.e., GASDALIE mutations enhanced and LALA mutations decreased ADCC) (Figure S4B). As expected due to the different epitopes they recognize, NTD for CV3-13 and S2 for CV3-25, a 1:1 cocktail of CV3-13 GASDALIE and CV3-25 LALA bound the spike at higher levels than when the individual antibodies were used at the maximum concentration (Figure S4A). Despite higher binding displayed by the cocktail, the ADCC and neutralizing activity was similar to the ADCC activity of CV3-13 GASDALIE alone and the neutralizing activity of CV3-25 LALA alone (Figures S4B and S4C). Thus, this cocktail recapitulates the desired effects of CV3-13 GASDALIE (high ADCC) and CV3-25 LALA (potent neutralization) but these functional activities are in separate entities. In agreement with previous results (Ullah et al., 2021b), CV3-25 LALA was unable to protect mice under a prophylactic regimen (Figures 7A–7F). Remarkably, when mice were pre-treated with a 1:1 combination of CV3-13 GASDALIE and CV3-25 LALA, we were unable to detect nLuc signals by BLI, suggesting complete inhibition of virus replication. Lack of body weight loss, viral loads below limit of detection in target organs, 100% survival, and near basal levels of inflammatory cytokine mRNA levels confirmed complete protection due to pretreatment with the combination of antibodies (Figures 7B–7J). Thus, despite the inability of CV3-13 GASDALIE and CV3-25 LALA to impact mortality in the face of lethal SARS-CoV-2 challenge when administered individually, their combination demonstrated complete protection using the stringent K18-hACE2 mouse model. Although GASDALIE mutations are not present in naturally occurring antibodies, our data suggest the significant synergistic potential of non-nAb in contributing toward SARS-CoV-2 immunity through their Fc-effector functions in the presence of nAb.

DISCUSSION

Neutralization plays a crucial role in protection against SARS-CoV-2 infection. Therefore many studies have focused on neutralization responses from convalescent plasma (Anand et al., 2021; Beaudoin-Bussieres et al., 2020; Gasser et al., 2021; Long et al., 2020; Prevost et al., 2020; Robbiani et al., 2020), vaccine-elicited antibodies (ClinicalTrials.gov: NCT04516746, NCT04368728, NCT04505722, NCT04470427; Baden et al., 2021; Polack et al., 2020; Skowronski and De Serres, 2021; Tauzin et al., 2021), and cocktails of mAbs for use as therapeutics (Hurlburt et al., 2020; Jennewein et al., 2021; Ju et al., 2020; Li et al., 2021b; Liu et al., 2020; Schafer et al., 2021; Tian et al., 2020; Wu et al., 2020b; Yuan et al., 2020). However, antibodies are polyvalent molecules able to mediate several antiviral functions (Adeniji et al., 2021). Among these, their capacity to recognize antigens at the surface of viral particles or infected cells and to recruit effector cells is gaining attention for SARS-CoV-2 infection (Brunet-Ratnasingham et al., 2021; Schafer et al., 2021; Tortorici et al., 2020; Ullah et al., 2021a; Winkler et al., 2021; Zohar et al., 2020). Also, recent studies on vaccine-elicited humoral responses suggest that additional mechanisms, besides neutralization, could be playing a role in vaccine efficacy (Alter et al., 2021; Amanat et al., 2021; Stankov et al., 2021; Tauzin et al., 2021). To address whether a non-nAb can contribute to SARS-CoV-2 immunity, we isolated a non-nAb,

(B) Representative images from BLI of SARS-CoV-2-nLuc-infected mice in ventral (v) as well as dorsal (d) positions and after necropsy at the indicated dpi for experiment as in (A).
(C) *Ex vivo* quantification of the nLuc signal as flux (photons/s) at 4 dpi after necropsy.
(D and E) Temporal quantification of the nLuc signal as flux (photons/s) computed non-invasively in indicated areas of each animal.
(F) Temporal changes in mouse body weight with initial body weight set to 100%.
(G and H) *Ex vivo* imaging of organs and quantification of the nLuc signal as flux (photons/s) at the indicated dpi after necropsy.
(I) Viral loads (nLuc activity/g) from indicated organs using Vero E6 cells as targets.
(J and K) Cytokine mRNA levels in lung and brain tissues after necropsy normalized to *Gapdh* in the same sample and that in uninfected mice. Scale bars in (B) and (G) denote radiance (photons/s/cm^2/steradian). Each curve in (D–F) and each data point in (C) and (H–J) represents an individual mouse. An equal number of female and male mice were used in each group. The group data in (C) and (H–K) were analyzed by two-way ANOVA followed by Tukey's multiple comparison tests. Statistical significance for group comparisons to control are shown in black, CV3-13 WT in red and CV3-13 GASDALIE in green. *$p < 0.05$, **$p < 0.01$, ***$p < 0.001$, ****$p < 0.0001$. Comparisons shown as "ns" or lacking * indicate non-significant statistical significance $p > 0.05$; mean values ± SD are depicted.

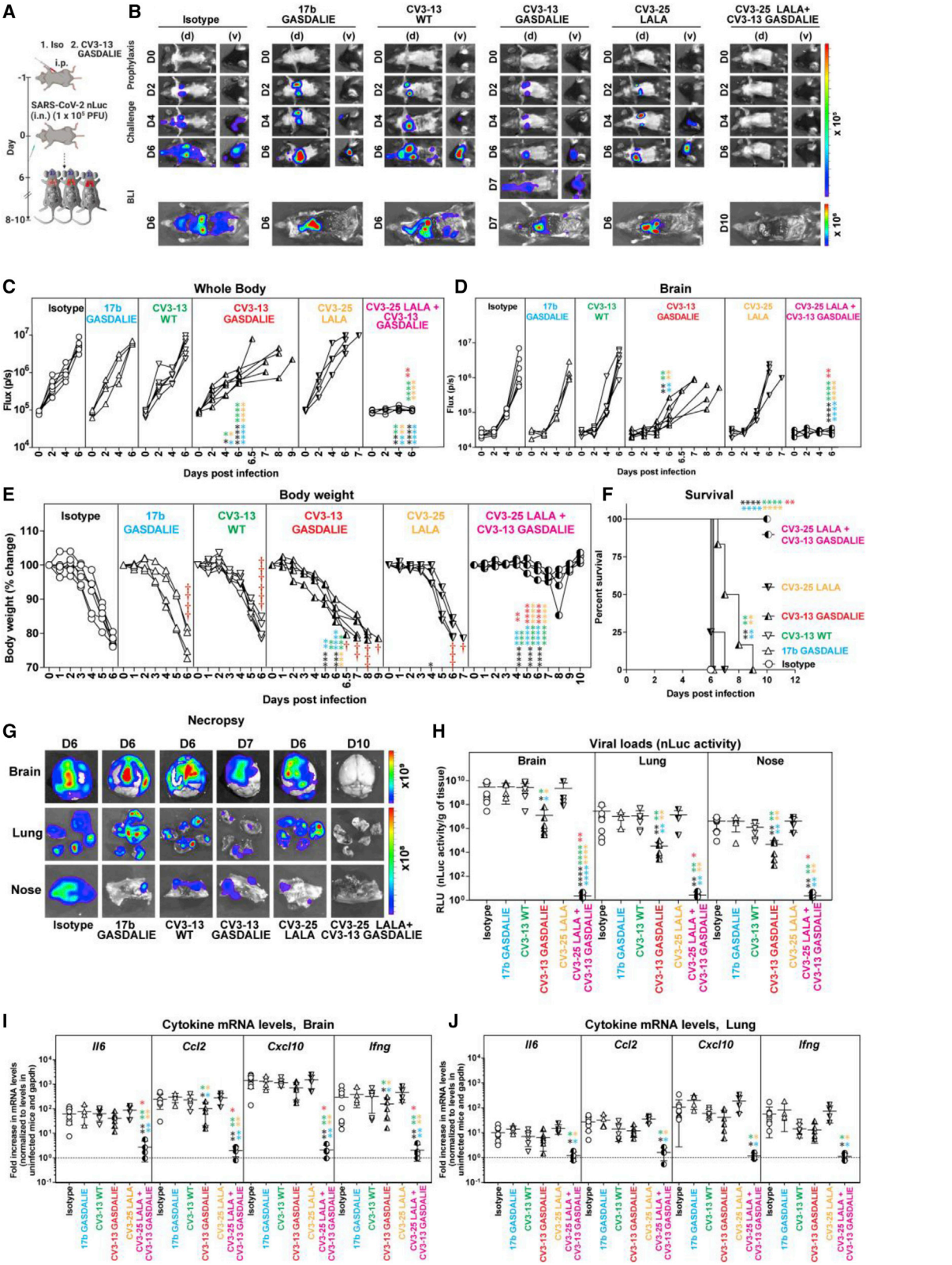

(legend on next page)

CV3-13, from a convalescent donor and assessed its impact on the virus replication *in vivo* in the K18-hACE2 mouse model. CV3-13 binds the NTD of the spike with high affinity and defines an NTD epitope. Compared with other NTD supersite-directed nAbs that bind the NTD predominantly through use of the N1, N3, and N5 loops and approach the NTD from the top, CV3-13 targets the lateral NTD surface, engaging and rearranging a set of antigenic NTD loops: N2, N4, and N2-3 hairpin. The NTD interface residues, as identified by the cryo-EM structure, harbor frequent mutations in several circulating SARS-CoV-2 variants, including B.1.1.7 (alpha), B.1.617.1 (kappa), C.37 (lambda), and B.1.1.529.1 (omicron), defining the structural basis for viral escape from CV3-13 and CV3-13-like antibodies. For instance, Tyr^{144} on the protruding N3 loop forms close contact with the Tyr/Phe-rich CDR H3 of CV3-13 (Figure 3D), and is deleted in B.1.1.7, which markedly reduces its binding to CV3-13 (Figure 1A). Other NTD mutations outside of the supersite are found within the CV3-13 epitope including an N2 deletion ^{69}HisVal^{70} in B.1.1.7, a Gly^{75} to Val/Thr^{76} to Ile double mutation in C.37, and a recurrent Thr^{95} to Ile mutation in B.1.526, B.1.617.1, and B.1.1.529.1 (Figure S2A). This is in line with the interpretation that NTD mutations from the emerging variants may be a result of NTD-directed antibody selection, which is compatible with the hypothesis that non-nAb against the NTD , such as CV3-13, influence virus evolution through Fc-mediated effector functions.

CV3-13 did not neutralize pseudoviral particles or authentic SARS-CoV-2 viruses but did mediate Fc-effector functions against spike-expressing cells. We suggest that differences in fine epitope specificity and the angle of approach used by CV3-13 as compared with neutralizing NTD-specific mAbs limit its ability to sterically hinder spike-co-receptor/auxiliary receptor interactions, the prefusion-to-postfusion transition of spike and/or membrane fusion as has been suggested as a neutralization mechanism for other NTD-binding antibodies. However, the mode of CV3-13 binding may enable recognition of antibody immune complex by effector cells and stimulate Fc-effector activities. Interestingly, we have previously shown that, for anti-HIV-1 non-nAbs, the precise epitope target and angle of approach by which an antibody attaches to the antigen are key factors contributing to the effectiveness of the Fc-mediated effector function (Acharya et al., 2014; Tolbert et al., 2019, 2020).

Our data demonstrate that an antibody devoid of neutralizing activity is able to reduce virus dissemination and delay death in mice from lethal SARS-CoV-2 challenge via its Fc-mediated effector functions. While WT CV3-13 IgG1 did not provide any protection, the CV3-13 GASDALIE mutant delayed death in prophylactically treated mice. These data suggest that a threshold of Fc-mediated effector function activity is required to decrease virus progression. When the non-nAb CV3-13 GASDALIE was combined with a nAb CV3-25 with impaired Fc functions, we observed complete protection in a stringent lethal challenge model. The mechanism behind the observed synergistic protection needs further elucidation. Depletion of specific innate immune cells will clarify the role of effector cells in antibody-mediated protection. In addition, our structural and functional analyses reveal that the combination of antibodies CV3-13 and CV3-25, which bind to different spike subunits, can function without negatively impacting the overall Fc-effector or neutralizing function of the mix (Figure S4). Thus, our results suggest that non-nAb have desirable functions that can synergize with nAbs to control viral replication *in vivo*.

While non-nAbs cannot directly inactivate free viruses, they remain attractive candidates for eliminating infected cells through Fc engagement and reduce virus burden. Although the characteristics including binding efficiency and angle of approach for efficient elimination of infected cells by non-nAbs remains to be elucidated, here we show that enhanced Fc mutations (GASDALIE) are a crucial step in improving *in vivo* efficacy.

Altogether, CV3-13 represents a class of non-nAb NTD-directed mAbs that can mediate Fc-effector functions both *in vivo* and *in vitro*. Our data indicate that, in addition to neutralization, additional antibody properties including Fc-mediated effector functions even from a non-nAb can contribute to SARS-CoV-2 immunity by limiting viral spread and infection.

Limitations of the study

We used K18-hACE2 mice as a model to study the impact of antibodies on SARS-CoV-2 replication. While K18-hACE2 mice

Figure 7. Fc-enhanced CV3-13 in combination with Fc-compromised nAb CV3-25 protects K18-hACE2 mice from lethal SARS-CoV-2 infection

(A) Experimental design for testing *in vivo* efficacy of indicated antibodies or combinations administered 1 day before challenging K18-hACE2 mice (i.n.) with SARS-CoV-2-nLuc followed by non-invasive BLI every 2 days. Human IgG (Iso) or HIV-1 co-receptor site binding 17b antibody carrying GASDALIE mutations (12.5 mg IgG/kg) were used as controls.

(B) Representative images from BLI of SARS-CoV-2-nLuc-infected mice in ventral (v) and dorsal (d) positions at the indicated dpi and after necropsy for experiment as in (A).

(C and D) Temporal quantification of the nLuc signal as flux (photons/s) computed non-invasively in indicated areas of each animal.

(E) Temporal changes in mouse body weight with initial body weight set to 100%. "†" denote mice that succumbed to infection.

(F) Kaplan-Meier survival curves of mice statistically compared by log rank (Mantel-Cox) test for experiment as in (A).

(G) *Ex vivo* imaging of indicated organs after necropsy.

(H) Viral loads (nLuc activity/g) from indicated organs using Vero E6 cells as targets.

(I and J) Cytokine mRNA levels in lung and brain tissues after necropsy normalized to *Gapdh* in the same sample and that in uninfected mice. Viral loads (H) and inflammatory cytokine profile (I and J) were determined after necropsy for mice when they succumbed to infection. Scale bars in (B) and (G) denote radiance (photons/s/cm^2/steradian). Each curve in (C–E) and each data point in (H–J) represents an individual mouse. An equal number of female and male mice were used in each group. The group data in (C–E) and (H–J) were analyzed by two-way ANOVA followed by Tukey's multiple comparison tests. Statistical significance for group comparisons to control are shown in black, 17b GASDALIE in blue, CV3-13 WT in green, CV3-13 GASDALIE in red, CV3-25 LALA in peach, and combination of CV3-25 LALA + CV3-13 GASDALIE in pink. *$p < 0.05$, **$p < 0.01$, ***$p < 0.001$, ****$p < 0.0001$. Comparisons shown as "ns" or lacking * indicate non-significant statistical comparisons $p > 0.05$; mean values ± SD are depicted.

display acute lung injury and cytokine storm that are hallmarks of SARS-CoV-2 infection, they succumb due to viral neuroinvasion that is not observed in humans. However, the extreme susceptibility of K18-hACE2 mice due to SARS-CoV-2 neuroinvasion sets a high bar for antiviral strategies that target virus replication and spread. Using Fc engineering as a tool, we have demonstrated a potential role for non-nAb in contributing to SARS-CoV-2 immunity when acting in concert with nAb. However, Fc-enhanced version of antibodies do not exist naturally. Therefore, the contribution of non-nAb in curbing SARS-CoV-2 replication needs further examination. Given that a large proportion of antibodies in convalescent plasma are non-neutralizers, there is a high likelihood that non-nAb with naturally high effector cell engagement exist that can synergize with nAb to boost SARS-CoV-2 immunity.

STAR★METHODS

Detailed methods are provided in the online version of this paper and include the following:

- KEY RESOURCES TABLE
- RESOURCE AVAILABILITY
  - Lead contact
  - Materials availability
  - Data and code availability
- EXPERIMENTAL MODEL AND SUBJECT DETAILS
  - Cell and viruses
  - Ethics statement
  - Antibodies
  - Mouse experiments
- METHOD DETAILS
  - SARS-CoV-2 infection and treatment conditions
  - Bioluminescence imaging (BLI) of SARS-CoV-2 infection
  - Measurement of viral burden
  - Analyses of signature inflammatory cytokines mRNA
  - Protein expression and purification
  - SARS-CoV-2 spike ELISA (enzyme-linked immunosorbent assay)
  - Flow cytometry analysis of cell-surface spike staining
  - Surface plasmon resonance (SPR)
  - Pseudovirus neutralization assay
  - Microneutralization assay
  - Cell-surface staining of SARS-CoV-2-infected cells
  - Cryo-immunohistology of organs
  - Antibody dependent cellular cytotoxicity (ADCC) assay
  - Antibody dependent cellular phagocytosis (ADCP) assay
  - Cryo-EM sample preparation and data collection
  - Cryo-EM data processing, model building and analysis
- QUANTIFICATION AND STATISTICAL ANALYSIS

SUPPLEMENTAL INFORMATION

Supplemental information can be found online at https://doi.org/10.1016/j.celrep.2022.110368.

ACKNOWLEDGMENTS

The authors thank the CRCHUM BSL-3 and Flow Cytometry Platforms for technical assistance. Antibodies CV3-1, CV3-13, and CV3-25 were produced using the pTT vector kindly provided by the National Research Council Canada. Schematics for showing experimental design in figures were created with BioRender.com. This work was supported by le Ministère de l'Économie et de l'Innovation (MEI) du Québec, the Fondation du CHUM, CIHR grant nos. 352417 and 177958, and a CFI grant, 41027, to A.F. Support was also provided by Sentinelle COVID Quebec to A.F. and M.R. NIH grant R01AI163395 to W.M. A.F. is recipient of a Canada Research Chair. G.B.-B. is the recipient of an FRQS PhD fellowship and J.P. is the recipient of a CIHR PhD fellowship. R.G. is supported by a Mitacs fellowship. The funders had no role in study design, data collection and analysis, decision to publish, or preparation of the manuscript. Cryo-EM data were collected at the Maryland Center for Advanced Molecular Analyses which is supported by MPOWER (The University of Maryland Strategic Partnership). The views expressed in this manuscript are those of the authors and do not reflect the official policy or position of the Uniformed Services University, the US Army, the Department of Defense, or the US Government.

AUTHOR CONTRIBUTIONS

Conceptualization, experimental design, interpretation, manuscript preparation and writing, G.B.-B., Y.C., I.U., P.D.U., M.P., and A.F.; generation of the GASDALIE and LALA mutants, figure generation, data processing, and initial draft, G.B.-B.; animal experiments, BLI, viral load analyses, data processing, and figure generation, I.U.; cryo-EM data collection, processing, and validation, Y.C., E.P., W.D.T., M.P., and F.Z.; structural analysis and figure generation, Y.C., W.D.T., and M.P.; histological analyses and figure generation, P.D.U.; isolation, generation, and characterization of SARS-CoV-2 S mAb CV3-13, G.B.-B., J.P., M.B., S.Y.G., S.D., R.G., Y.C., A.T., G.G., L.S., D.V., D.C., A.T.McG., J.R., M.P., W.M., and A.F.; generation of the individual B.1.1.7 mutations in the spike, S.Y.G., J.P., and D.V.; provided authentic SARS-CoV-2 virus, M.R. and H.C.; funding for the work, P.K., M.P., P.D.U., W.M., and A.F. All authors read, edited, and approved the final manuscript.

DECLARATION OF INTERESTS

L.S., A.T.M., and A.F. have filed a provisional patent application on the following monoclonal antibodies: CV3-1, CV3-13, and CV3-25.

Received: September 8, 2021
Revised: December 16, 2021
Accepted: January 20, 2022
Published: January 25, 2022

REFERENCES

Acharya, P., Tolbert, W.D., Gohain, N., Wu, X., Yu, L., Liu, T., Huang, W., Huang, C.C., Kwon, Y.D., Louder, R.K., et al. (2014). Structural definition of an antibody-dependent cellular cytotoxicity response implicated in reduced risk for HIV-1 infection. J. Virol. *88*, 12895–12906.

Adeniji, O.S., Giron, L.B., Purwar, M., Zilberstein, N.F., Kulkarni, A.J., Shaikh, M.W., Balk, R.A., Moy, J.N., Forsyth, C.B., Liu, Q., et al. (2021). COVID-19 severity is associated with differential antibody Fc-mediated innate immune functions. mBio *12*, e00281–21.

Alter, G., Gorman, M., Patel, N., Guebre-Xabier, M., Zhu, A., Atyeo, C., Pullen, K., Loos, C., Goez-Gazi, Y., Carrion, R., et al. (2021). Collaboration between the Fab and Fc contribute to maximal protection against SARS-CoV-2 following NVX-CoV2373 subunit vaccine with Matrix-M vaccinationPreprint at. Res. Sq. https://doi.org/10.21203/rs.3.rs-200342/v1.

Amanat, F., Thapa, M., Lei, T., Ahmed, S.M.S., Adelsberg, D.C., Carreno, J.M., Strohmeier, S., Schmitz, A.J., Zafar, S., Zhou, J.Q., et al. (2021). The plasmablast response to SARS-CoV-2 mRNA vaccination is dominated by

non-neutralizing antibodies that target both the NTD and the RBDPreprint at. medRxiv. https://doi.org/10.1101/2021.03.07.21253098.

Amraie, R., Napoleon, M.A., Yin, W., Berrigan, J., Suder, E., Zhao, G., Olejnik, J., Gummuluru, S., Muhlberger, E., Chitalia, V., et al. (2020). CD209L/L-SIGN and CD209/DC-SIGN act as receptors for SARS-CoV-2 and are differentially expressed in lung and kidney epithelial and endothelial cellsPreprint at. bioRxiv. https://doi.org/10.1101/2020.06.22.165803.

Anand, S.P., Prevost, J., Nayrac, M., Beaudoin-Bussieres, G., Benlarbi, M., Gasser, R., Brassard, N., Laumaea, A., Gong, S.Y., Bourassa, C., et al. (2021). Longitudinal analysis of humoral immunity against SARS-CoV-2 spike in convalescent individuals up to 8 months post-symptom onset. Cell Rep. Med. *2*, 100290.

Baden, L.R., El Sahly, H.M., Essink, B., Kotloff, K., Frey, S., Novak, R., Diemert, D., Spector, S.A., Rouphael, N., Creech, C.B., et al. (2021). Efficacy and safety of the mRNA-1273 SARS-CoV-2 vaccine. N. Engl. J. Med. *384*, 403–416.

Barad, B.A., Echols, N., Wang, R.Y., Cheng, Y., DiMaio, F., Adams, P.D., and Fraser, J.S. (2015). EMRinger: side chain-directed model and map validation for 3D cryo-electron microscopy. Nat. Methods *12*, 943–946.

Beaudoin-Bussieres, G., Laumaea, A., Anand, S.P., Prevost, J., Gasser, R., Goyette, G., Medjahed, H., Perreault, J., Tremblay, T., Lewin, A., et al. (2020). Decline of humoral responses against SARS-CoV-2 spike in convalescent individuals. mBio *11*, e02590–20.

Beaudoin-Bussieres, G., Richard, J., Prevost, J., Goyette, G., and Finzi, A. (2021). A new flow cytometry assay to measure antibody-dependent cellular cytotoxicity against SARS-CoV-2 spike-expressing cells. STAR Protoc. *2*, 100851.

Bournazos, S., Klein, F., Pietzsch, J., Seaman, M.S., Nussenzweig, M.C., and Ravetch, J.V. (2014). Broadly neutralizing anti-HIV-1 antibodies require Fc effector functions for in vivo activity. Cell *158*, 1243–1253.

Bournazos, S., DiLillo, D.J., Goff, A.J., Glass, P.J., and Ravetch, J.V. (2019). Differential requirements for FcgammaR engagement by protective antibodies against Ebola virus. Proc Natl Acad Sci U S A *116*, 20054–20062.

Brunet-Ratnasingham, E., Anand, S.P., Gantner, P., Moquin-Beaudry, G., Dyachenko, A., Brassard, N., Beaudoin-Bussières, G., Pagliuzza, A., Gasser, R., Benlarbi, M., et al. (2021). Integrated immunovirological profiling validates plasma SARS-CoV-2 RNA as an early predictor of COVID-19 mortality. Sci. Adv. *7*, eabj5629.

Buchrieser, J., Dufloo, J., Hubert, M., Monel, B., Planas, D., Rajah, M.M., Planchais, C., Porrot, F., Guivel-Benhassine, F., Van der Werf, S., et al. (2020). Syncytia formation by SARS-CoV-2-infected cells. EMBO J. *39*, e106267.

Burnley, T., Palmer, C.M., and Winn, M. (2017). Recent developments in the CCP-EM software suite. Acta Crystallogr. D Struct. Biol. *73*, 469–477.

Cao, Y., Su, B., Guo, X., Sun, W., Deng, Y., Bao, L., Zhu, Q., Zhang, X., Zheng, Y., Geng, C., et al. (2020). Potent neutralizing antibodies against SARS-CoV-2 identified by high-throughput single-cell sequencing of convalescent patients' B cells. Cell *182*, 73–84.e16.

Cerutti, G., Guo, Y., Zhou, T., Gorman, J., Lee, M., Rapp, M., Reddem, E.R., Yu, J., Bahna, F., Bimela, J., et al. (2021). Potent SARS-CoV-2 neutralizing antibodies directed against spike N-terminal domain target a single supersite. Cell Host Microbe. *29*, 819–833.e817.

Chen, V.B., Arendall, W.B., 3rd, Headd, J.J., Keedy, D.A., Immormino, R.M., Kapral, G.J., Murray, L.W., Richardson, J.S., and Richardson, D.C. (2010). MolProbity: all-atom structure validation for macromolecular crystallography. Acta Crystallogr. D Biol. Crystallogr. *66*, 12–21.

Chen, X., Li, R., Pan, Z., Qian, C., Yang, Y., You, R., Zhao, J., Liu, P., Gao, L., Li, Z., et al. (2020). Human monoclonal antibodies block the binding of SARS-CoV-2 spike protein to angiotensin converting enzyme 2 receptor. Cell Mol Immunol *17*, 647–649.

Chi, X., Yan, R., Zhang, J., Zhang, G., Zhang, Y., Hao, M., Zhang, Z., Fan, P., Dong, Y., Yang, Y., et al. (2020). A neutralizing human antibody binds to the N-terminal domain of the spike protein of SARS-CoV-2. Science *369*, 650–655.

Dekkers, G., Bentlage, A.E.H., Stegmann, T.C., Howie, H.L., Lissenberg-Thunnissen, S., Zimring, J., Rispens, T., and Vidarsson, G. (2017). Affinity of human IgG subclasses to mouse Fc gamma receptors. MAbs *9*, 767–773.

DiLillo, D.J., and Ravetch, J.V. (2015). Differential Fc-receptor engagement drives an anti-tumor vaccinal effect. Cell *161*, 1035–1045.

DiLillo, D.J., Tan, G.S., Palese, P., and Ravetch, J.V. (2014). Broadly neutralizing hemagglutinin stalk-specific antibodies require FcgammaR interactions for protection against influenza virus in vivo. Nat Med *20*, 143–151.

Ding, S., Adam, D., Beaudoin-Bussières, G., Tauzin, A., Gong, S.Y., Gasser, R., Laumaea, A., Anand, S.P., Privé, A., Bourassa, C., et al. (2021). SARS-CoV-2 Spike Expression at the Surface of Infected Primary Human Airway Epithelial Cells. Viruses *14*, 5.

Duan, L., Zheng, Q., Zhang, H., Niu, Y., Lou, Y., and Wang, H. (2020). The SARS-CoV-2 spike glycoprotein biosynthesis, structure, function, and antigenicity: implications for the design of spike-based vaccine immunogens. Front. Immunol. *11*, 576622.

Dunbar, J., Krawczyk, K., Leem, J., Marks, C., Nowak, J., Regep, C., Georges, G., Kelm, S., Popovic, B., and Deane, C.M. (2016). SAbPred: a structure-based antibody prediction server. Nucleic Acids Res. *44*, W474–W478.

Durocher, Y., Perret, S., and Kamen, A. (2002). High-level and high-throughput recombinant protein production by transient transfection of suspension-growing human 293-EBNA1 cells. Nucleic Acids Res. *30*, E9.

Emary, K.R.W., Golubchik, T., Aley, P.K., Ariani, C.V., Angus, B., Bibi, S., Blane, B., Bonsall, D., Cicconi, P., Charlton, S., et al. (2021). Efficacy of ChAdOx1 nCoV-19 (AZD1222) vaccine against SARS-CoV-2 variant of concern 202012/01 (B.1.1.7): an exploratory analysis of a randomised controlled trial. Lancet *397*, 1351–1362.

Emsley, P., and Cowtan, K. (2004). Coot: model-building tools for molecular graphics. Acta Crystallogr. D Biol. Crystallogr. *60*, 2126–2132.

Emsley, P., Lohkamp, B., Scott, W.G., and Cowtan, K. (2010). Features and development of Coot. Acta Crystallogr. D Biol. Crystallogr. *66*, 486–501.

Gasser, R., Cloutier, M., Prevost, J., Fink, C., Ducas, E., Ding, S., Dussault, N., Landry, P., Tremblay, T., Laforce-Lavoie, A., et al. (2021). Major role of IgM in the neutralizing activity of convalescent plasma against SARS-CoV-2. Cell Rep. *34*, 108790.

Goddard, T.D., Huang, C.C., and Ferrin, T.E. (2007). Visualizing density maps with UCSF Chimera. J. Struct. Biol. *157*, 281–287.

Goddard, T.D., Huang, C.C., Meng, E.C., Pettersen, E.F., Couch, G.S., Morris, J.H., and Ferrin, T.E. (2018). UCSF ChimeraX: meeting modern challenges in visualization and analysis. Protein Sci. *27*, 14–25.

Harvey, W.T., Carabelli, A.M., Jackson, B., Gupta, R.K., Thomson, E.C., Harrison, E.M., Ludden, C., Reeve, R., Rambaut, A., Consortium, C.-G.U., et al. (2021). SARS-CoV-2 variants, spike mutations and immune escape. Nat. Rev. Microbiol. *19*, 409–424.

Hoffmann, M., Kleine-Weber, H., Schroeder, S., Kruger, N., Herrler, T., Erichsen, S., Schiergens, T.S., Herrler, G., Wu, N.H., Nitsche, A., et al. (2020). SARS-CoV-2 cell entry depends on ACE2 and TMPRSS2 and is blocked by a clinically proven protease inhibitor. Cell *181*, 271–280.e8.

Hsieh, C.L., Goldsmith, J.A., Schaub, J.M., DiVenere, A.M., Kuo, H.C., Javanmardi, K., Le, K.C., Wrapp, D., Lee, A.G., Liu, Y., et al. (2020). Structure-based design of prefusion-stabilized SARS-CoV-2 spikes. Science *369*, 1501–1505.

Hurlburt, N.K., Seydoux, E., Wan, Y.H., Edara, V.V., Stuart, A.B., Feng, J., Suthar, M.S., McGuire, A.T., Stamatatos, L., and Pancera, M. (2020). Structural basis for potent neutralization of SARS-CoV-2 and role of antibody affinity maturation. Nat. Commun. *11*, 5413.

Jennewein, M.F., MacCamy, A.J., Akins, N.R., Feng, J., Homad, L.J., Hurlburt, N.K., Seydoux, E., Wan, Y.H., Stuart, A.B., Edara, V.V., et al. (2021). Isolation and characterization of cross-neutralizing coronavirus antibodies from COVID-19+ subjects. Cell Rep. *36*, 109353.

Ju, B., Zhang, Q., Ge, J., Wang, R., Sun, J., Ge, X., Yu, J., Shan, S., Zhou, B., Song, S., et al. (2020). Human neutralizing antibodies elicited by SARS-CoV-2 infection. Nature *584*, 115–119.

Krissinel, E., and Henrick, K. (2007). Inference of macromolecular assemblies from crystalline state. J. Mol. Biol. *372*, 774–797.

Lan, J., Ge, J., Yu, J., Shan, S., Zhou, H., Fan, S., Zhang, Q., Shi, X., Wang, Q., Zhang, L., et al. (2020). Structure of the SARS-CoV-2 spike receptor-binding domain bound to the ACE2 receptor. Nature *581*, 215–220.

Lazar, G.A., Dang, W., Karki, S., Vafa, O., Peng, J.S., Hyun, L., Chan, C., Chung, H.S., Eivazi, A., Yoder, S.C., et al. (2006). Engineered antibody Fc variants with enhanced effector function. Proc. Natl. Acad. Sci. U S A *103*, 4005–4010.

Lempp, F.A., Soriaga, L., Montiel-Ruiz, M., Benigni, F., Noack, J., Park, Y.-J., Bianchi, S., Walls, A.C., Bowen, J.E., Zhou, J., et al. (2021). Membrane lectins enhance SARS-CoV-2 infection and influence the neutralizing activity of different classes of antibodiesPreprint at. bioRxiv. https://doi.org/10.1101/2021.04.03.438258.

Li, D., Edwards, R.J., Manne, K., Martinez, D.R., Schafer, A., Alam, S.M., Wiehe, K., Lu, X., Parks, R., Sutherland, L.L., et al. (2021a). In vitro and in vivo functions of SARS-CoV-2 infection-enhancing and neutralizing antibodies. Cell *184*, 4203–4219.e32.

Li, W., Chen, Y., Prevost, J., Ullah, I., Lu, M., Gong, S.Y., Tauzin, A., Gasser, R., Vezina, D., Anand, S.P., et al. (2021b). Structural basis and mode of action for two broadly neutralizing antibodies against SARS-CoV-2 emerging variants of concernPreprint at. bioRxiv. https://doi.org/10.1101/2021.08.02.454546.

Liebschner, D., Afonine, P.V., Baker, M.L., Bunkoczi, G., Chen, V.B., Croll, T.I., Hintze, B., Hung, L.W., Jain, S., McCoy, A.J., et al. (2019). Macromolecular structure determination using X-rays, neutrons and electrons: recent developments in Phenix. Acta Crystallogr. D Struct. Biol. *75*, 861–877.

Liu, L., Wang, P., Nair, M.S., Yu, J., Rapp, M., Wang, Q., Luo, Y., Chan, J.F., Sahi, V., Figueroa, A., et al. (2020). Potent neutralizing antibodies against multiple epitopes on SARS-CoV-2 spike. Nature *584*, 450–456.

Liu, Y., Soh, W.T., Kishikawa, J.I., Hirose, M., Nakayama, E.E., Li, S., Sasai, M., Suzuki, T., Tada, A., Arakawa, A., et al. (2021). An infectivity-enhancing site on the SARS-CoV-2 spike protein targeted by antibodies. Cell *184*, 3452–3466.e18.

Long, Q.X., Tang, X.J., Shi, Q.L., Li, Q., Deng, H.J., Yuan, J., Hu, J.L., Xu, W., Zhang, Y., Lv, F.J., et al. (2020). Clinical and immunological assessment of asymptomatic SARS-CoV-2 infections. Nat. Med. *26*, 1200–1204.

Lu, M., Uchil, P.D., Li, W., Zheng, D., Terry, D.S., Gorman, J., Shi, W., Zhang, B., Zhou, T., Ding, S., et al. (2020). Real-time conformational dynamics of SARS-CoV-2 spikes on virus particles. Cell Host Microbe *28*, 880–891 e888.

Luchsinger, L.L., Ransegnola, B.P., Jin, D.K., Muecksch, F., Weisblum, Y., Bao, W., George, P.J., Rodriguez, M., Tricoche, N., Schmidt, F., et al. (2020). Serological assays estimate highly variable SARS-CoV-2 neutralizing antibody activity in recovered COVID-19 patients. J. Clin. Microbiol *58*, e02005–20.

McCallum, M., De Marco, A., Lempp, F.A., Tortorici, M.A., Pinto, D., Walls, A.C., Beltramello, M., Chen, A., Liu, Z., Zatta, F., et al. (2021). N-terminal domain antigenic mapping reveals a site of vulnerability for SARS-CoV-2. Cell *184*, 2332–2347.e16.

McCarthy, K.R., Rennick, L.J., Nambulli, S., Robinson-McCarthy, L.R., Bain, W.G., Haidar, G., and Duprex, W.P. (2021). Recurrent deletions in the SARS-CoV-2 spike glycoprotein drive antibody escape. Science *371*, 1139–1142.

ter Meulen, J., van den Brink, E.N., Poon, L.L., Marissen, W.E., Leung, C.S., Cox, F., Cheung, C.Y., Bakker, A.Q., Bogaards, J.A., van Deventer, E., et al. (2006). Human monoclonal antibody combination against SARS coronavirus: synergy and coverage of escape mutants. PLoS Med. *3*, e237.

Muecksch, F., Wise, H., Batchelor, B., Squires, M., Semple, E., Richardson, C., McGuire, J., Clearly, S., Furrie, E., Greig, N., et al. (2021). Longitudinal serological analysis and neutralizing antibody levels in coronavirus disease 2019 convalescent patients. J. Infect. Dis. *223*, 389–398.

Oliver, S.E., Gargano, J.W., Marin, M., Wallace, M., Curran, K.G., Chamberland, M., McClung, N., Campos-Outcalt, D., Morgan, R.L., Mbaeyi, S., et al. (2021a). The advisory committee on immunization practices' interim recommendation for use of moderna COVID-19 vaccine—United States, December 2020. MMWR Morb Mortal Wkly Rep. *69*, 1653–1656.

Oliver, S.E., Gargano, J.W., Scobie, H., Wallace, M., Hadler, S.C., Leung, J., Blain, A.E., McClung, N., Campos-Outcalt, D., Morgan, R.L., et al. (2021b). The advisory committee on immunization practices' interim recommendation for use of Janssen COVID-19 vaccine—United States, February 2021. MMWR Morb Mortal Wkly Rep. *70*, 329–332.

Payne, D.C., Smith-Jeffcoat, S.E., Nowak, G., Chukwuma, U., Geibe, J.R., Hawkins, R.J., Johnson, J.A., Thornburg, N.J., Schiffer, J., Weiner, Z., et al. (2020). SARS-CoV-2 infections and serologic responses from a sample of U.S. Navy service members—USS Theodore Roosevelt, April 2020. MMWR Morb Mortal Wkly Rep. *69*, 714–721.

Pettersen, E.F., Goddard, T.D., Huang, C.C., Meng, E.C., Couch, G.S., Croll, T.I., Morris, J.H., and Ferrin, T.E. (2021). UCSF ChimeraX: structure visualization for researchers, educators, and developers. Protein Sci. *30*, 70–82.

Pfizer/BioNTech (2021). Pfizer and BioNTech Confirm High Efficacy and No Serious Safety Concerns through up to Six Months Following Second Dose in Updated Topline Analysis of Landmark COVID-19 Vaccine Study. https://www.pfizer.com/news/press-release/press-release-detail/pfizer-and-biontech-confirm-high-efficacy-and-no-serious.

Piccoli, L., Park, Y.J., Tortorici, M.A., Czudnochowski, N., Walls, A.C., Beltramello, M., Silacci-Fregni, C., Pinto, D., Rosen, L.E., Bowen, J.E., et al. (2020). Mapping neutralizing and immunodominant sites on the SARS-CoV-2 spike receptor-binding domain by structure-guided high-resolution serology. Cell *183*, 1024–1042 e1021.

Polack, F.P., Thomas, S.J., Kitchin, N., Absalon, J., Gurtman, A., Lockhart, S., Perez, J.L., Perez Marc, G., Moreira, E.D., Zerbini, C., et al. (2020). Safety and efficacy of the BNT162b2 mRNA COVID-19 vaccine. N. Engl. J. Med. *383*, 2603–2615.

Prevost, J., Gasser, R., Beaudoin-Bussieres, G., Richard, J., Duerr, R., Laumaea, A., Anand, S.P., Goyette, G., Benlarbi, M., Ding, S., et al. (2020). Cross-sectional evaluation of humoral responses against SARS-CoV-2 spike. Cell Rep Med *1*, 100126.

Prevost, J., Richard, J., Gasser, R., Ding, S., Fage, C., Anand, S.P., Adam, D., Vergara, N.G., Tauzin, A., Benlarbi, M., et al. (2021). Impact of temperature on the affinity of SARS-CoV-2 spike for ACE2Preprint at. bioRxiv. https://doi.org/10.1101/2021.07.09.451812.

Punjani, A., Rubinstein, J.L., Fleet, D.J., and Brubaker, M.A. (2017). cryoSPARC: algorithms for rapid unsupervised cryo-EM structure determination. Nat. Methods *14*, 290–296.

Rappazzo, C.G., Tse, L.V., Kaku, C.I., Wrapp, D., Sakharkar, M., Huang, D., Deveau, L.M., Yockachonis, T.J., Herbert, A.S., Battles, M.B., et al. (2021). Broad and potent activity against SARS-like viruses by an engineered human monoclonal antibody. Science *371*, 823–829.

Richards, J.O., Karki, S., Lazar, G.A., Chen, H., Dang, W., and Desjarlais, J.R. (2008). Optimization of antibody binding to FcgammaRIIa enhances macrophage phagocytosis of tumor cells. Mol. Cancer Ther. *7*, 2517–2527.

Robbiani, D.F., Gaebler, C., Muecksch, F., Lorenzi, J.C.C., Wang, Z., Cho, A., Agudelo, M., Barnes, C.O., Gazumyan, A., Finkin, S., et al. (2020). Convergent antibody responses to SARS-CoV-2 in convalescent individuals. Nature *584*, 437–442.

Rubinstein, J.L., and Brubaker, M.A. (2015). Alignment of cryo-EM movies of individual particles by optimization of image translations. J. Struct. Biol. *192*, 188–195.

Saunders, K.O. (2019). Conceptual approaches to modulating antibody effector functions and circulation half-life. Front. Immunol. *10*, 1296.

Schafer, A., Muecksch, F., Lorenzi, J.C.C., Leist, S.R., Cipolla, M., Bournazos, S., Schmidt, F., Maison, R.M., Gazumyan, A., Martinez, D.R., et al. (2021). Antibody potency, effector function, and combinations in protection and therapy for SARS-CoV-2 infection in vivo. J. Exp. Med. *218*, e20201993.

Scheres, S.H., and Chen, S. (2012). Prevention of overfitting in cryo-EM structure determination. Nat. Methods *9*, 853–854.

Seydoux, E., Homad, L.J., MacCamy, A.J., Parks, K.R., Hurlburt, N.K., Jennewein, M.F., Akins, N.R., Stuart, A.B., Wan, Y.H., Feng, J., et al. (2020). Analysis of a SARS-CoV-2-infected individual reveals development of potent neutralizing antibodies with limited somatic mutation. Immunity *53*, 98–105 e105.

Shang, J., Wan, Y., Luo, C., Ye, G., Geng, Q., Auerbach, A., and Li, F. (2020). Cell entry mechanisms of SARS-CoV-2. Proc. Natl. Acad. Sci. U S A. *117*, 11727–11734.

Skowronski, D.M., and De Serres, G. (2021). Safety and efficacy of the BNT162b2 mRNA COVID-19 vaccine. N. Engl. J. Med. *384*, 1576–1577.

Smith, P., DiLillo, D.J., Bournazos, S., Li, F., and Ravetch, J.V. (2012). Mouse model recapitulating human Fcgamma receptor structural and functional diversity. Proc. Natl. Acad. Sci. U S A *109*, 6181–6186.

Soh, W.T., Liu, Y., Nakayama, E.E., Ono, C., Torii, S., Nakagami, H., Matsuura, Y., Shioda, T., and Arase, H. (2020). The N-terminal domain of spike glycoprotein mediates SARS-CoV-2 infection by associating with L-SIGN and DC-SIGNPreprint at. bioRxiv. https://doi.org/10.1101/2020.11.05.369264.

Stankov, M.V., Cossmann, A., Bonifacius, A., Dopfer-Jablonka, A., Ramos, G.M., Gödecke, N., Scharff, A.Z., Happle, C., Boeck, A.-L., Tran, A.T., et al. (2021). Humoral and cellular immune responses against SARS-CoV-2 variants and human coronaviruses after single BNT162b2 vaccination. Clin. Infect. Dis.

Sun, Y., Wang, L., Feng, R., Wang, N., Wang, Y., Zhu, D., Xing, X., Yang, P., Zhang, Y., Li, W., et al. (2021). Structure-based development of three- and four-antibody cocktails against SARS-CoV-2 via multiple mechanisms. Cell Res. *31*, 597–600.

Suryadevara, N., Shrihari, S., Gilchuk, P., VanBlargan, L.A., Binshtein, E., Zost, S.J., Nargi, R.S., Sutton, R.E., Winkler, E.S., Chen, E.C., et al. (2021). Neutralizing and protective human monoclonal antibodies recognizing the N-terminal domain of the SARS-CoV-2 spike protein. Cell *184*, 2316–2331.e15.

Tauzin, A., Nayrac, M., Benlarbi, M., Gong, S.Y., Gasser, R., Beaudoin-Bussieres, G., Brassard, N., Laumaea, A., Vezina, D., Prevost, J., et al. (2021). A single dose of the SARS-CoV-2 vaccine BNT162b2 elicits Fc-mediated antibody effector functions and T cell responses. Cell Host Microbe *29*, 1137–1150.e6.

The PyMOL Molecular Graphics System, Version 1.2r3pre, Schrödinger, LLC

Tian, X., Li, C., Huang, A., Xia, S., Lu, S., Shi, Z., Lu, L., Jiang, S., Yang, Z., Wu, Y., et al. (2020). Potent binding of 2019 novel coronavirus spike protein by a SARS coronavirus-specific human monoclonal antibody. Emerg. Microbes Infect. *9*, 382–385.

Tolbert, W.D., Sherburn, R.T., Van, V., and Pazgier, M. (2019). Structural basis for epitopes in the gp120 cluster A region that invokes potent effector cell activity. Viruses *11*, 69.

Tolbert, W.D., Sherburn, R., Gohain, N., Ding, S., Flinko, R., Orlandi, C., Ray, K., Finzi, A., Lewis, G.K., and Pazgier, M. (2020). Defining rules governing recognition and Fc-mediated effector functions to the HIV-1 co-receptor binding site. BMC Biol. *18*, 91.

Tortorici, M.A., Beltramello, M., Lempp, F.A., Pinto, D., Dang, H.V., Rosen, L.E., McCallum, M., Bowen, J., Minola, A., Jaconi, S., et al. (2020). Ultrapotent human antibodies protect against SARS-CoV-2 challenge via multiple mechanisms. Science *370*, 950–957.

Ullah, I., Prevost, J., Ladinsky, M.S., Stone, H., Lu, M., Anand, S.P., Beaudoin-Bussieres, G., Symmes, K., Benlarbi, M., Ding, S., et al. (2021a). Live imaging of SARS-CoV-2 infection in mice reveals neutralizing antibodies require Fc function for optimal efficacy, Preprint at. bioRxiv.

Ullah, I., Prevost, J., Ladinsky, M.S., Stone, H., Lu, M., Anand, S.P., Beaudoin-Bussieres, G., Symmes, K., Benlarbi, M., Ding, S., et al. (2021b). Live imaging of SARS-CoV-2 infection in mice reveals that neutralizing antibodies require Fc function for optimal efficacy. Immunity *54*, 2143–2158 e2115.

Voss, W.N., Hou, Y.J., Johnson, N.V., Delidakis, G., Kim, J.E., Javanmardi, K., Horton, A.P., Bartzoka, F., Paresi, C.J., Tanno, Y., et al. (2021). Prevalent, protective, and convergent IgG recognition of SARS-CoV-2 non-RBD spike epitopes. Science *372*, 1108–1112.

Voysey, M., Clemens, S.A.C., Madhi, S.A., Weckx, L.Y., Folegatti, P.M., Aley, P.K., Angus, B., Baillie, V.L., Barnabas, S.L., Bhorat, Q.E., et al. (2021). Safety and efficacy of the ChAdOx1 nCoV-19 vaccine (AZD1222) against SARS-CoV-2: an interim analysis of four randomised controlled trials in Brazil, South Africa, and the UK. Lancet *397*, 99–111.

Walls, A.C., Park, Y.J., Tortorici, M.A., Wall, A., McGuire, A.T., and Veesler, D. (2020). Structure, function, and antigenicity of the SARS-CoV-2 spike glycoprotein. Cell *181*, 281–292 e286.

Wang, C., Li, W., Drabek, D., Okba, N.M.A., van Haperen, R., Osterhaus, A., van Kuppeveld, F.J.M., Haagmans, B.L., Grosveld, F., and Bosch, B.J. (2020). A human monoclonal antibody blocking SARS-CoV-2 infection. Nat. Commun. *11*, 2251.

Winkler, E.S., Gilchuk, P., Yu, J., Bailey, A.L., Chen, R.E., Chong, Z., Zost, S.J., Jang, H., Huang, Y., Allen, J.D., et al. (2021). Human neutralizing antibodies against SARS-CoV-2 require intact Fc effector functions for optimal therapeutic protection. Cell *184*, 1804–1820 e1816.

Wrapp, D., De Vlieger, D., Corbett, K.S., Torres, G.M., Wang, N., Van Breedam, W., Roose, K., van Schie, L., VIB-CMB COVID-19 Response Team; and Hoffmann, M., et al. (2020a). Structural basis for potent neutralization of betacoronaviruses by single-domain camelid antibodies. Cell *181*, 1004–1015.e15.

Wrapp, D., Wang, N., Corbett, K.S., Goldsmith, J.A., Hsieh, C.L., Abiona, O., Graham, B.S., and McLellan, J.S. (2020b). Cryo-EM structure of the 2019-nCoV spike in the prefusion conformation. Science *367*, 1260–1263.

Wu, F., Liu, M., Wang, A., Lu, L., Wang, Q., Gu, C., Chen, J., Wu, Y., Xia, S., Ling, Y., et al. (2020a). Evaluating the association of clinical characteristics with neutralizing antibody levels in patients who have recovered from mild COVID-19 in Shanghai, China. JAMA Intern. Med. *180*, 1356–1362.

Wu, Y., Wang, F., Shen, C., Peng, W., Li, D., Zhao, C., Li, Z., Li, S., Bi, Y., Yang, Y., et al. (2020b). A noncompeting pair of human neutralizing antibodies block COVID-19 virus binding to its receptor ACE2. Science *368*, 1274–1278.

Xie, X., Muruato, A., Lokugamage, K.G., Narayanan, K., Zhang, X., Zou, J., Liu, J., Schindewolf, C., Bopp, N.E., Aguilar, P.V., et al. (2020a). An infectious cDNA clone of SARS-CoV-2. Cell Host Microbe *27*, 841–848.e3.

Xie, X., Muruato, A.E., Zhang, X., Lokugamage, K.G., Fontes-Garfias, C.R., Zou, J., Liu, J., Ren, P., Balakrishnan, M., Cihlar, T., et al. (2020b). A nanoluciferase SARS-CoV-2 for rapid neutralization testing and screening of anti-infective drugs for COVID-19. Nat. Commun. *11*, 5214.

Yuan, M., Wu, N.C., Zhu, X., Lee, C.D., So, R.T.Y., Lv, H., Mok, C.K.P., and Wilson, I.A. (2020). A highly conserved cryptic epitope in the receptor binding domains of SARS-CoV-2 and SARS-CoV. Science *368*, 630–633.

Zivanov, J., Nakane, T., Forsberg, B.O., Kimanius, D., Hagen, W.J., Lindahl, E., and Scheres, S.H. (2018). New tools for automated high-resolution cryo-EM structure determination in RELION-3. eLife *7*, e42166.

Zivanov, J., Nakane, T., and Scheres, S.H.W. (2019). A Bayesian approach to beam-induced motion correction in cryo-EM single-particle analysis. IUCrJ *6*, 5–17.

Zohar, T., Loos, C., Fischinger, S., Atyeo, C., Wang, C., Slein, M.D., Burke, J., Yu, J., Feldman, J., Hauser, B.M., et al. (2020). Compromised humoral functional evolution tracks with SARS-CoV-2 mortality. Cell *183*, 1508–1519.e12.

STAR★METHODS

KEY RESOURCES TABLE

REAGENT or RESOURCE	SOURCE	IDENTIFIER
Antibodies		
InVivoMAb human IgG1 isotype control	Bio X Cell	RRID: AB_2687817 Cat # BE0297
Cross-reactive SARS-CoV-1 monoclonal antibody CR3022	ter Meulen et al. (2006)	RRID: AB_2848080
CV3-1 (hIgG1)	Jennewein et al. (2021)	N/A
CV3-13 (hIgG1)	Jennewein et al. (2021)	N/A
CV3-25 (hIgG1)	Jennewein et al. (2021)	N/A
CV3-13 LALA (hIgG1)	Finzi Lab, Université de Montréal	N/A
CV3-25 LALA (hIgG1)	Finzi Lab, Université de Montréal	N/A
CV3-13 GASDALIE (hIgG1)	Finzi Lab, Université de Montréal	N/A
17b GASDALIE (hIgG1)	Finzi Lab, Université de Montréal	N/A
Goat anti-Human IgG (H + L) Cross-Adsorbed Secondary Antibody, Alexa Fluor 647	Invitrogen	Cat # A-21445; RRID: AB_2535862
Goat anti-Human IgG Fc Cross-Adsorbed Secondary Antibody, HRP	Invitrogen	Cat # A18823; RRID: AB_2535600
Mouse anti-SARS-CoV-2 nucleocapsid (clone 1C7)	Bioss Antibodies	Cat # bsm-41411M
Alexa Fluor® 488 anti-SARS-CoV-2 nucleocapsid (mBG17)	Prevost et al. (2021)	N/A
Rabbit anti-SARS-CoV-2 nucleocapsid	Novus	Cat # NB100-56576
Goat anti-Human IgG Fc Cross-Adsorbed Secondary Antibody, HRP	Invitrogen	Cat # 31413; RRID: AB_429693
Bacterial and virus strains		
SARS-CoV-2-nLuc (strain 2019-nCoV/USA_WA1/2020)	Craig B. Wilen (Yale University)	K. Plante and Pei-Yong Shi, World Reference Center for Emerging Viruses and Arboviruses, University of Texas Medical Branch)
Authentic SARS-CoV-2 D614G virus (LSPQ/231457/2020)	Prevost et al. (2021)	N/A
Biological samples		
Primary human peripheral blood mononuclear cells (PBMCs)	FRQS AIDS network	N/A
Chemicals, peptides, and recombinant proteins		
Liberase TL Research Grade	Sigma-Aldrich	Cat# 5401020001
DNAse I recombinant, RNAse-free	Roche	Ref # 04716728001
Gibco™ RPMI 1640 medium	Thermo Fisher Scientific	Cat # 11875093
Gibco™ Dulbecco's modified Eagle's medium (DMEM)	Thermo Fisher Scientific	Cat # 11965118
Gibco™ MEM Non-essential amino acid (NEAA) solution	Thermo Fisher Scientific	Cat # 11140050
Gibco™ Penicillin-streptomycin solution (10,000 U/ml)	Thermo Fisher Scientific	Cat # 15140122
Gibco™ Dulbecco's Phosphate Buffered Saline (DPBS)	Thermo Fisher Scientific	Cat # 14190144
Gibco™ L-Glutamine (200 mM)	Thermo Fisher Scientific	Cat # 25030081
Gibco™ 0.05% Trypsin-EDTA, phenol red	Thermo Fisher Scientific	Cat # 25300054
Fetal bovine serum	Atlanta Biologicals	Cat # S11550
RBC Lysis Buffer (10X)	BioLegend Inc	Cat # 420301

(*Continued on next page*)

Continued

REAGENT or RESOURCE	SOURCE	IDENTIFIER
Bovine Serum Albumin (BSA)	Sigma-Aldrich	Cat# A9647-100G CAS: 9048-46-8
Accutase	BioLegend Inc	Cat # 423201
0.05% Trypsin-EDTA (1X)	Life Technologies	Cat # 25300-054
K3 EDTA 15% Solution	Fisher Scientific	Cat # BD 366450
Sodium pyruvate (100 mM)	Life technologies	Ref # 11360-070
2-Mercaptoethanol	Sigma-Aldrich	Cat # M3148
L-Glutamine (200 mM)	Life technologies	Ref # 25030-081
Red blood cell lysis buffer-Hybri-Max	Sigma-Aldrich	Cat # R7757-100ML
Tris-buffered saline (TBS)	Thermo Fisher Scientific	Cat # BP24711
Western Lightning Plus-ECL, Enhanced Chemiluminescence Substrate	Perkin Elmer Life Sciences	Cat # NEL105001EA
Tween20	Thermo Fisher Scientific	Cat # BP337-500
Passive lysis buffer	Promega	Cat # E1941
Triton-X 100 t-octyl phenoxy polyethoxyethanol	American Bioanalytical	Cat # AB02025-00500 CAS: 9002-93-1
Paraformaldehyde (PFA)	Electron Microscopy Sciences	Cat # 19200 CAS: 30525-89-4
Rat serum	Stemcell Biotechnologies	Cat # 13551
L-lysine Monohydrochloride	Sigma-Aldrich	Cat # L1262
Sodium (meta)periodate	Sigma-Aldrich	Cat # 30323-100G CAS: 7790-28-5
Sucrose/ α-D-glucopyranosyl-β-D-fructofuranoside	americanBIO	Ref # AB01900-01000 CAS: 57-50-1
Tissue-Tek O.C.T Compound	Sakura	Cat # 4583
Fc receptor blocker	Innovex	Cat # NB335-5
Superforst® Plus microscope slides	Thermo Scientific	Cat # 4951PLUS-001
Dimethyl sulfoxide (DMSO)	Sigma-Aldrich	Cat # D2650-5X5ML CAS: 67-68-5
Sodium azide	Sigma-Aldrich	Cat # S-8032 EC No: 247-852-1
Sodium phosphate, Monobasic, Monohydrate, Crystal ($NaH_2PO_4 \cdot H_2O$)	J.T.Baker	Cat # 3818-01 CAS: 10049-21-5
Sodium phosphate, Dibasic, Anhydrous (Na_2HPO_4)	J.T.Baker	Cat # 3828-01 CAS: 7558-79-4
Glycine	American Bioanalytical	Cat # AB00730-01000 CAS: 56-40-6
The PEG-it Virus precipitation solution (5X)	System Bioscience	Cat # LV810A-1
Avicel® Pharma Grade	FMC	Cat # RC-581 NF 10.20944/preprints202005.0264.v1
Vector® TrueView® Autofluorescence Quenching Kit	Vector Laboratories	SP-8400
Puromycin dihydrochloride	Millipore Sigma	Cat # P8833
D-Luciferin potassium salt	Prolume	Cat # 306
Formaldehyde 37%	Thermo Fisher Scientific	Cat # F79-500
LIVE/DEAD Fixable AquaVivid Cell Stain	Thermo Fisher Scientific	Cat # L34957
Cell proliferation dye eFluor670	Thermo Fisher Scientific	Cat # 65-0840-85
Cell proliferation dye eFluor450	Thermo Fisher Scientific	Cat # 65-0842-85
FreeStyle 293F expression medium	ThermoFisher Scientific	Cat # 12338002
ExpiFectamine 293 transfection reagent	ThermoFisher Scientific	Cat # A14525
Protein A Sepharose CL-4B	Cytiva	Cat # 17096303
Ni-NTA agarose	Invitrogen	Cat # R90110

(*Continued on next page*)

Continued

REAGENT or RESOURCE	SOURCE	IDENTIFIER
Papain-agarose resin	ThermoFisher Scientific	Cat # 20341
SARS-CoV-2 S1 domain C-His tag protein, from HEK293 cells	BEI Resources	NR-53798
SARS-CoV-2 S2 ectodomain C-His tag protein, from Baculovirus	BEI Resources	NR-53799
SIGMAFAST OPD	EMD Millipore	Cat # P9187
Critical commercial assays		
Nano-Glo Luciferase Assay System (nanoluc substrate)	Promega	Cat # N1120
Pierce™ Gaussia Luciferase Glow Assay Kit	ThermoFisher Scientific	Cat # 16160
Strep-Tactin®XT 4Flow	IBA Lifesciences	Cat # 2-5998-000
KAPA SYBR FAST qPCR Master Mix (2X) Kit	KAPA Biosystems	Cat # KK4600 and KK4601
Ambion DNase I (RNase-free)	ThermoFisher Scientific	Cat # AM2222
RNeasy Mini Kit (50)	Qiagen	Cat #/ID 74104
iScript advanced cDNA kit	Bio Rad	Cat #1725038
iQ Multiplex Powermix	Bio Rad	Cat # 1725848
iScript™ cDNA Synthesis Kit	Bio Rad	Cat # 95047-100
Deposited Data		
structure of CV3-13 Fab with SARS-CoV-2 spike	Protein Data Bank	7RQ6
structure of CV3-13 Fab with SARS-CoV-2 spike	Electron Microscopy Data Bank	EMD-24628
Experimental models: Cell lines		
Vero E6 (female, Chlorocebus sabaeus)	ATCC	Cat # CRL-1586; RRID: CVCL_0574
Vero E6-TMPRSS2 (female, Chlorocebus sabaeus)	Craig B. Wilen, Yale University	N/A
HEK293 (female, Homo sapiens)	ATCC	Cat # CRL-1573; RRID: CVCL_0045
HEK293T (female, Homo sapiens)	ATCC	Cat # CRL-3216; RRID: CVCL_0063
Expi293F™ GnTI- Cells (female, Homo sapiens)	ThermoFisher Scientific	Cat # A39240; RRID: CVCL_B0J7
Expi293F cells (female, Homo sapiens)	ThermoFisher Scientific	Cat # A14527; RRID: CVCL_D615
293T-ACE2 (female, Homo sapiens)	Prevost et al., (2020) (Prevost et al., 2020)	N/A
CEM.NKr-CCR5+ (female, Homo sapiens)	NIH AIDS Reagent Program	Cat # 4376; RRID: CVCL_X623
CEM.NKr-Spike (female, Homo sapiens)	Anand et al. (2021)	N/A
THP-1 (male, Homo sapiens)	ATCC	Cat # TIB-202; RRID: CVCL_0006
FreeStyle 293F cells (female, Homo sapiens)	ThermoFisher Scientific	Cat # R79007; RRID: CVCL_D603
Experimental models: Organisms/strains		
B6.Cg-Tg(K18-ACE2)2Prlmn/J (males and females) 6-8 weeks old	The Jackson Laboratory	Stock No: 034860 RRID: IMSR_JAX: 034860
Oligonucleotides		
SARS-CoV-2 N F: 5′-ATGCTGCAA TCGTGCTACAA-3′	Yale School of Medicine, W. M. Keck Foundation, Oligo Synthesis Resource	N/A
SARS-CoV-2 N R: 5′-GACTGC CGCCTCTGCTC-3′	Yale School of Medicine, W. M. Keck Foundation, Oligo Synthesis Resource	N/A
Human IgG1 G236A-S239D F : 5′-CTCCTGGCGGGA CCGGATGTCTTCCTCTTC-3′	Integrated DNA Technologies	N/A
Human IgG1 G236A-S239D R : 5′-GAAGAGGAAGACA TCCGGTCCCGCCAGGAG-3′	Integrated DNA Technologies	N/A
Human IgG1 A330L-I332E F : 5′-GCCCTCCCACTCCC CGAAGAGAAAACCATC-3′	Integrated DNA Technologies	N/A

(*Continued on next page*)

Continued

REAGENT or RESOURCE	SOURCE	IDENTIFIER
Human IgG1 A330L-I332E R : 5′-GATGGTTTTCTCTTCGG GGAGTGGGAGGGC-3′	Integrated DNA Technologies	N/A
Human IgG1 L234A-L235A F: 5′-CAGCACCTGAAGCCGC GGGGGGACCGTC-3′	Integrated DNA Technologies	N/A
Human IgG1 L234A-L235A R: 5′-GACGGTCCCCCCGC GGCTTCAGGTGCTG-3′	Integrated DNA Technologies	N/A
FAM-GAPDH	Bio Rad	Cat # 12001950
HEX-IL6	Bio Rad	Cat # 10031228
TEX615-CCL2	Bio Rad	Cat # 10031234
Cy5-CXCL10	Bio Rad	Cat # 10031231
Cy5.5-IFNg	Bio Rad	Cat # 10031237
Transgene Forward: GAC CCC TGA GGG TTT CAT ATA G	Yale School of Medicine, W. M. Keck Foundation, Oligo Synthesis Resource	#53437, Genotyping primers for K18-hACE2 mice. The Jackson Laboratory
Common: CAC CAA CAC AGT TTC CCA AC	Yale School of Medicine, W. M. Keck Foundation, Oligo Synthesis Resource	#53438, Genotyping primers for K18-hACE2 mice. The Jackson Laboratory
Wildtype forward: AAG TTG GAG AAG ATG CTG AAA GA	Yale School of Medicine, W. M. Keck Foundation, Oligo Synthesis Resource	#53439, Genotyping primers for K18-hACE2 mice. The Jackson Laboratory
Recombinant DNA		
pCMV-SARS-CoV-2 Spike D614G Δ19	Ullah et al. (2021a)	N/A
pCMV-SARS-CoV-2 Spike	Sino Biological	Cat # VG40589-UT
pCMV delta R8.2	Addgene	Cat #12263
HIV-1-inGluc-ΔEnv	Mothes Lab, Yale University	N/A
pCG1-SARS-CoV-2 Spike	Hoffmann et al. (2020)	N/A
pCG1-SARS-CoV-2 Spike D614G	Beaudoin-Bussieres et al. (2020)	N/A
pCG1-SARS-CoV-2 Spike D614G N501Y	Prevost et al. (2021)	N/A
pcDNA3.1-SARS-CoV-2 Spike B.1.1.7	Tauzin et al. (2021)	N/A
pCG1-SARS-CoV-2 Spike D614G Δ69-70	Li et al. (2021b)	N/A
pCG1-SARS-CoV-2 Spike D614G Δ144	Li et al. (2021b)	N/A
pCG1-SARS-CoV-2 Spike D614G A570D	Li et al. (2021b)	N/A
pCG1-SARS-CoV-2 Spike D614G P681H	Li et al. (2021b)	N/A
pCG1-SARS-CoV-2 Spike D614G T716I	Li et al. (2021b)	N/A
pCG1-SARS-CoV-2 Spike D614G S982A	Li et al. (2021b)	N/A
pCG1-SARS-CoV-2 Spike D614G D1118H	Li et al. (2021b)	N/A
pαH-SARS-CoV-2 Spike HexaPro	Dr Jason S. McLellan, University of Texas	N/A
pcDNA3.1-SARS-CoV-2 RBD	Beaudoin-Bussieres et al. (2020)	N/A
pNL4.3 R-E- Luc	NIH AIDS Reagent Program	Cat # 3418
pIRES2-eGFP vector	Clontech	Cat # 6029-1
Software and algorithms		
FlowJo v10.5.3	Treestar	https://www.flowjo.com/
Nikon-Elements AR Analysis v4.13 and Acquisition v4.5	Nikon	N/A
Adobe Photoshop CC	Adobe Systems Inc	N/A
Adobe Illustrator CC	Adobe Systems Inc	N/A
BioRender (schematics in figures)	BioRender.com	N/A

(*Continued on next page*)

Continued

REAGENT or RESOURCE	SOURCE	IDENTIFIER
CFX MaestroTM Software (qPCR analyses)	Bio-rad Inc	N/A
Graphpad Prism v9.0.1	GraphPad Software	https://www.graphpad.com/
SerialEM software package	David N. Mastronarde, University of Colorado Boulder	https://bio3d.colorado.edu/SerialEM/
IMOD software package	David N. Mastronarde, University of Colorado Boulder	https://bio3d.colorado.edu/imod/
CryoSPARC	Punjani et al. (2017)	https://cryosparc.com
Phenix	Liebschner et al. (2019)	https://phenix-online.org/
Coot	Emsley et al. (2010)	https://www2.mrc-lmb.cam.ac.uk/personal/pemsley/coot/
Relion	Scheres and Chen (2012); Zivanov et al.(2018, 2019)	https://www2.mrc-lmb.cam.ac.uk/relion/index.php?title=Main_Page
UCSF ChimeraX	Goddard et al. (2018)	https://www.rbvi.ucsf.edu/chimerax/
UCSF Chimera	Goddard et al. (2007)	http://plato.cgl.ucsf.edu/chimera RRID: SCR_004097
PyMOL	The PyMOL Molecular Graphics System	https://www.schrodinger.com/products/pymol
MolProbity	Chen et al. (2010)	http://molprobity.biochem.duke.edu/
PISA	Krissinel and Henrick (2007)	https://www.ebi.ac.uk/pdbe/pisa/
Gen5 microplate reader and imager software	Biotek	N/A
BIAevaluation software	GE Healthcare	Cat # BR-1005-97
Other		
TriStar LB 941 Multimode Microplate Reader and Luminometer	BERTHOLD TECHNOLOGIES GmbH & Co. KG	Finzi and Mothes Lab
Evos M7000 Imaging system	Invitrogen	Mothes and Ho lab, Yale university
Leica Cryostat CM1950	Leica	CM1950 (Ya-Chi HoLab; Yale Unviersity)
Nikon W1 Spinning Disk Confocal microscope	Nikon Instruments Inc, Americas	Yale West Campus Imaging Core
C1000 Touch thermal cycler	Bio-Rad	N/A
CFX Connect™ Real-Time PCR Detection System	Bio-Rad	N/A
Nanodrop Spectrophotometer ND-1000	ThermoFisher Scientific	N/A
27G × ½'' insulin syringe with needle	TERUMO	Cat # SS*05M2713
31G insulin syringe	BD Biosciences	Cat # 328468
70 μm Nylon cell strainer	FALCON	Cat # 352350
Acrodisc 25 mm Syringe Filter w/0.45 μm HT Tuffryn Membrane	PALL Life Sciences	Cat # 4184
Superfrost Plus Microscope Slides	Thermo Scientific	Cat # 4951PLUS-001
96-well white plates for luciferase assays	Costar	Cat # 3917
Accu-Edge High Profile Microtome Blades	SAKURA	Cat # 4685
Microcover glasses 1 ounce No.1	VWR	Cat # 48393 106
Tissue-Tek Cryomold	SAKURA	Ref # 4557
Brass planchettes	Ted Pella, Inc.	Type A and Type B
Cryotubes	Thermo Scientific Nunc	Cat # 340711
Teflon-coated glass microscope slides		N/A
Microsurgical scalpel	Electron Microscopy Sciences	Cat # 72047-15
Plastic sectioning stubs	Home Made	N/A
Diamond knife	Diatome, Ltd	N/A
Formvar-coated copper-rhodium slot grids	Electron Microscopy Sciences	N/A
Dual-axis tomography holder	E.A. Fischione Instruments, Export PA	Model 2040

(*Continued on next page*)

Continued

REAGENT or RESOURCE	SOURCE	IDENTIFIER
Polystyrene Round-bottom Tube	FALCON	Ref # 352058
Optical Flat 8-Cap Strips for 0.2 mL tube stripes/plates	Bio-Rad	Cat # TCS0803
Individual PCR tubes 8-tube Strip, clear	Bio-Rad	Cat # TLS0801
ThermalGrid Rigid Strip PCR tubes	Denville Scientific INC	Ref # C18064
96 well U bottom plate	FALCON	Ref # 353077
XIC-3 animal isolation chamber	PerkinElmer	N/A
IVIS Spectrum	PerkinElmer	Yale University ABSL-3 facility
RAS-4 Rodent Anesthesia System	PerkinElmer	CLS146737
QUANTIFOIL® holey carbon grids	Electron Microscopy Sciences	Cat # Q250-CR1
Synergy LX multi-mode reader	Biotek	N/A
Superose 6 10/300 GL	GE Healthcare	Cat # 17517201
Hiload 16/600 Superdex 200pg	GE Healthcare	Cat # 28989335
Biacore 3000	GE Healthcare	N/A
Protein A sensor chip	Cytiva	Cat # 29127558
Ni-NTA sensor chip	Cytiva	Cat # BR100034

RESOURCE AVAILABILITY

Lead contact

Further information and requests for resources and reagents should be directed to and will be fulfilled by the Lead Contact, Andrés Finzi (andres.finzi@umontreal.ca).

Materials availability

All other unique reagents generated in this study are available from the corresponding authors with a completed Materials Transfer Agreement.

Data and code availability

- All data reported in this paper will be shared by the lead contact (andres.finzi@umontreal.ca) upon request.
- The cryoelectron microscopy structure of CV3-13 in complex with the SARS-CoV-2 spike is deposited in the Protein Data Bank (PDB) with accession code 7RQ6 and in the Electron Microscopy Data Bank (EMDB) with accession code EMD-24628
- Any additional information required to reanalyze the data reported in this paper is available from the lead contact (andres.finzi@umontreal.ca) upon request.

EXPERIMENTAL MODEL AND SUBJECT DETAILS

Cell and viruses

Vero E6 (CRL-1586, American Type Culture Collection (ATCC) or Vero E6-TMPRSS2 (Craig B. Wilen, Yale University), were cultured at 37°C in RPMI supplemented with 10% fetal bovine serum (FBS), 10 mM HEPES pH 7.3, 1 mM sodium pyruvate, 1× non-essential amino acids, and 100 U/ml of penicillin–streptomycin. The 2019n-CoV/USA_WA1/2019 isolate of SARS-CoV-2 expressing nanoluciferase was obtained from Craig Wilen, Yale University and generously provided by K. Plante and Pei-Yong Shi, World Reference Center for Emerging Viruses and Arboviruses, University of Texas Medical Branch) (Xie et al., 2020a, 2020b). Virus was propagated in Vero-E6 or Vero E6-TMPRSS2 by infecting them in T150 cm^2 flasks at a MOI of 0.1. The culture supernatants were collected after 72 h when cytopathic effects were clearly visible. The cell debris was removed by centrifugation and filtered through 0.45-micron filter to generate virus stocks. Viruses were concentrated by adding one volume of cold (4°C) 4x PEG-it Virus Precipitation Solution (40% (w/v) PEG-8000 and 1.2 M NaCl; System Biosciences) to three volumes of virus-containing supernatant. The solution was mixed by inverting the tubes several times and then incubated at 4°C overnight. The precipitated virus was harvested by centrifugation at 1,500 × g for 60 min at 4°C. The concentrated virus was then resuspended in PBS then aliquoted for storage at −80°C. All work with infectious SARS-CoV-2 was performed in Institutional Biosafety Committee approved BSL3 and A-BSL3 facilities at Yale University School of Medicine or Université de Montréal using appropriate positive pressure air respirators and protective equipment. CEM.NKr, CEM.NKr-Spike, THP-1 and peripheral blood mononuclear cells (PBMCs) were maintained at 37°C under

5% CO_2 in RPMI media, supplemented with 10% FBS and 100 U/mL penicillin/streptomycin. 293T (or HEK293T) and 293T-ACE2 cells were maintained at 37°C under 5% CO_2 in DMEM media, supplemented with 5% FBS and 100 U/mL penicillin/streptomycin. CEM.NKr (NIH AIDS Reagent Program) is a T lymphocytic cell line resistant to NK cell-mediated lysis. CEM.NKr-Spike stably expressing SARS-CoV-2 Spike were used as target cells in ADCC and ADCP assays (Anand et al., 2021). THP-1 monocytic cell line (ATCC) was used as effector cells in the ADCP assay. PBMCs were obtained from healthy donor through leukapheresis and were used as effector cells in ADCC assay. 293T cells (obtained from ATCC) were derived from 293 cells, into which the simian virus 40 T-antigen was inserted. 293T-ACE2 cells stably expressing human ACE2 is derived from 293T cells (Prevost et al., 2020). 293T-ACE2 cells were cultured in medium supplemented with 2 mg/mL of puromycin (Millipore Sigma).

Ethics statement

PBMCs from healthy individuals as a source of effector cells in our ADCC assay were obtained under CRCHUM institutional review board (protocol #19.381). Research adhered to the standards indicated by the Declaration of Helsinki. All participants were adults and provided informed written consent prior to enrollment in accordance with Institutional Review Board approval.

Antibodies

The human antibodies (CV3-1, CV3-25 and CV3-13) used in the work were isolated from blood of male convalescent donor CV3 recovered 41 days after symptoms onset using fluorescent recombinant stabilized Spike ectodomains (S2P) as probes to identify antigen-specific B cells as previously described (Lu et al., 2020; Seydoux et al., 2020). Light and heavy chains were cloned into the pTT expression plasmid (Durocher et al., 2002). Site-directed mutagenesis was performed on plasmids expressing CV3-13, CV3-25 or 17b antibody heavy chains in order to introduce the LALA mutations (L234A/L235A) and/or the GASDALIE mutations (G236A/S239D/A330L/I332E) using to the QuickChange II XL site-directed mutagenesis protocol (Stratagene).

Mouse experiments

All experiments were approved by the Institutional Animal Care and Use Committees (IACUC) of and Institutional Biosafety Committee of Yale University (IBSCYU). All the animals were housed under specific pathogen-free conditions in the facilities provided and supported by Yale Animal Resources Center (YARC). All IVIS imaging, blood draw and virus inoculation experiments were done under anesthesia using regulated flow of isoflurane:oxygen mix to minimize pain and discomfort to the animals. The B6.Cg-Tg(K18-ACE2) 2Prlmn/J mice used for the experiments were between 6 and 8 weeks old. An equal number of male and female mice were used in each group of mice.

METHOD DETAILS

SARS-CoV-2 infection and treatment conditions

For all *in vivo* experiments, the 6 to 8 weeks male and female hACE2-K18 mice were intranasally challenged with 1×10^5 PFU in 25–30 μL volume under anesthesia (0.5 - 5% isoflurane delivered using precision Dräger vaporizer with oxygen flow rate of 1 L/min). For mAb treatment using prophylaxis regimen, mice were treated with 250 μg (12.5 μg/g body weight) of indicated antibodies (17b GASDALIE, CV3-13 WT or CV3-13 GASDALIE, CV3-25 LALA) via intraperitoneal injection (i.p.) 24 h prior to infection. For mAb treatment under therapeutic regimen, mice were treated at 1 and 2 dpi intraperitoneally with CV3-13 (12.5 μg/g body weight). Body weight was measured and recorded daily. The starting body weight was set to 100%. For survival experiments, mice were monitored every 6-12 h starting six days after virus administration. Lethargic and moribund mice or mice that had lost more than 20% of their body weight were sacrificed and considered to have succumbed to infection for Kaplan-Meier survival plots.

Bioluminescence imaging (BLI) of SARS-CoV-2 infection

All standard operating procedures and protocols for IVIS imaging of SARS-CoV-2 infected animals under ABSL-3 conditions were approved by IACUC, IBSCYU and YARC. All the imaging was carried out using IVIS Spectrum® (PerkinElmer) in XIC-3 animal isolation chamber (PerkinElmer) that provided biological isolation of anesthetized mice or individual organs during the imaging procedure. All mice were anesthetized via isoflurane inhalation (3 - 5% isoflurane, oxygen flow rate of 1.5 L/min) prior and during BLI using the XGI-8 Gas Anesthesia System. Prior to imaging, 100 μL of nanoluciferase substrate, furimazine (NanoGlo™, Promega, Madison, WI) diluted 1:40 in endotoxin-free PBS was retro-orbitally administered to mice under anesthesia. The mice were then placed into XIC-3 animal isolation chamber (PerkinElmer) pre-saturated with isothesia and oxygen mix. The mice were imaged in both dorsal and ventral position at indicated days post infection. The animals were then imaged again after euthanasia and necropsy by spreading additional 200 μL of substrate on to exposed intact organs. Infected areas of interest identified by carrying out whole-body imaging after necropsy were isolated, washed in PBS to remove residual blood and placed onto a clear plastic plate. Additional droplets of furimazine in PBS (1:40) were added to organs and soaked in substrate for 1-2 min before BLI.

Images were acquired and analyzed with the manufacturer's Living Image v4.7.3 *in vivo* software package. Image acquisition exposures were set to auto, with imaging parameter preferences set in order of exposure time, binning, and f/stop, respectively. Images were acquired with luminescent f/stop of 2, photographic f/stop of 8. Binning was set to medium. Comparative images were compiled and batch-processed using the image browser with collective luminescent scales. Photon flux was measured as

luminescent radiance (p/sec/cm^2/sr). During luminescent threshold selection for image display, luminescent signals were regarded as background when minimum threshold levels resulted in displayed radiance above non-tissue-containing or known uninfected regions. To determine the pattern of virus spread, the image sequences were acquired every day following administration of SARS-CoV-2 (i.n). Image sequences were assembled and converted to videos using Image J.

Measurement of viral burden

Indicated organs (nasal cavity, brain, lungs from infected or uninfected mice were collected, weighed, and homogenized in 1 mL of serum free RPMI media containing penicillin-streptomycin and homogenized in 2 mL tube containing 1.5 mm Zirconium beads with BeadBug 6 homogenizer (Benchmark Scientific, TEquipment Inc). Virus titers were measured using two highly correlative methods. First, the total RNA was extracted from homogenized tissues using RNeasy plus Mini kit (QIAGEN Cat # 74136), reverse transcribed with iScript advanced cDNA kit (Bio-Rad Cat #1725036) followed by a SYBR Green Real-time PCR assay for determining copies of SARS-CoV-2 N gene RNA using primers SARS-CoV-2 N F: 5′-ATGCTGCAATCGTGCTACAA-3′ and SARS-CoV-2 N R: 5′-GACTGCCGCCTCTGCTC-3′. RNA extracted from the corresponding tissues of uninfected mice were used for normalization of N mRNA copy numbers. We observe a Ct value ranging between 38 and 40 in uninfected samples with our primer set and conditions. Therefore we used a Ct value of 38 (lower end) to normalize all the data for estimating N RNA levels.

Second, serially diluted clarified tissue homogenates were used to infect Vero-E6 cell culture monolayer. We used nanoluciferase activity as a shorter surrogate for plaque assay. Infected cells were washed with PBS and then lysed using 1X Passive lysis buffer. The lysates transferred into a 96-well solid white plate (Costar Inc) and nanoluciferase activity was measured using Tristar multiwell Luminometer (Berthold Technology, Bad Wildbad, Germany) for 2.5 s by adding 20 μL of Nano-Glo® substrate in nanoluc assay buffer (Promega Inc, WI, USA). Uninfected monolayer of Vero cells treated identically served as controls to determine basal luciferase activity to obtain normalized relative light units. The data were processed and plotted using GraphPad Prism 8 v8.4.3.

Analyses of signature inflammatory cytokines mRNA

Brain and lung samples were collected from mice at the time of necropsy. Approximately, 20 mg of tissue was suspended in 500 μL of RLT lysis buffer, and RNA was extracted using RNeasy plus Mini kit (Qiagen Cat # 74136), reverse transcribed with iScript advanced cDNA kit (Bio-Rad Cat #1725036). To determine levels of signature inflammatory cytokines, multiplex qPCR was conducted using iQ Multiplex Powermix (Bio Rad Cat # 1725848) and PrimePCR Probe Assay mouse primers FAM-GAPDH, HEX-IL6, TEX615-CCL2, Cy5-CXCL10, and Cy5.5-IFNgamma. The reaction plate was analyzed using CFX96 touch real time PCR detection system. Scan mode was set to all channels. The PCR conditions were 95°C 2 min, 40 cycles of 95°C for 10 s and 60°C for 45 s, followed by a melting curve analysis to ensure that each primer pair resulted in amplification of a single PCR product. mRNA levels of Il6, Ccl2, Cxcl10 and Ifng in the cDNA samples of infected mice were normalized to gapdh with the formula ΔC_t(target gene) = C_t(target gene)-C_t(gapdh). The fold increase was determined using $2^{-\Delta\Delta Ct}$ method comparing treated mice to uninfected controls.

Protein expression and purification

FreeStyle 293F cells (Thermo Fisher) were grown in FreeStyle 293F medium (Thermo Fisher) to a density of 1x10^6 cells/mL at 37°C with 8% CO_2 with regular agitation (135 rpm). Cells were transfected with a plasmid coding for recombinant stabilized SARS-CoV-2 ectodomain (residue 1-1208) (S-6P or HexaPro Spike; obtained from Dr. Jason S. McLellan) (Hsieh et al., 2020), his-tagged SARS-CoV-2 RBD (residue 319-541) or SARS-CoV RBD-SD1(residue 306-577) using polyethylenimine (PEI). One-week post-transfection, supernatants were clarified and filtered using a 0.22 μm filter (Thermo Fisher Scientific). The crude S-6P was purified on strep-tactin resin (IBA) followed by size-exclusion chromatography on Superose 6 10/300 column (GE Healthcare) in 10 mM Tris pH 8.0 and 200 mM NaCl (SEC buffer). RBD was purified on a Ni-NTA column (Invitrogen) followed by size-exclusion chromatography on a Hiload 16/600 Superdex 200pg column using the same SEC buffer. For CryoEM protein sample preparation, the expression plasmid encoding S-6P was transfected into 293F GnT1-cells using PEI. The protein was harvested and purified with the same protocol as above. The C-terminal twin-Strep-Tag and 8xHis tag on S-6P was removed by HRV3C (Sigma) digestion as described in (Wrapp et al., 2020b) and the cleaved protein was further purified on a Ni-NTA column followed by gel filtration on a Superose 6 10/300 in SEC buffer. Purified proteins were snap-frozen in liquid nitrogen and stored in aliquots at −80°C until further use. Protein purity was confirmed by SDS-PAGE.

The expression plasmids encoding the heavy and light chains of CV3-13 IgG were transiently transfected into Expi293F cells (Thermo Fisher) using ExpiFectamine 293 transfection reagent as per the manufacturer's protocol (Thermo Fisher). After 6-days post-transfection, the antibody was purified on Protein A resin from cell supernatant (Thermo Fisher) before the overnight papain digestion at 37°C using immobilized papain agarose (Thermo Fisher). The resulting Fab was separated from Fc and undigested IgG by passage over protein A resin. Fab was further purified by gel filtration using a Superose 6 10/300 column before use in SPR binding or cryo-EM sample preparation.

FreeStyle 293F cells (Thermo Fisher) were grown in FreeStyle 293F medium (Thermo Fisher Scientific) to a density of 1x10^6 cells/mL at 37°C with 8% CO_2 with regular agitation (135 rpm). The expression plasmids encoding the heavy and light chains of 17b GASDALIE, CV3-1, CV3-25, CV3-25 LALA, CV3-13 WT, CV3-13 LALA and CV3-13 GASDALIE IgG were transfected into Freestyle 293F cells (Thermo Fisher Scientific) using ExpiFectamine 293 transfection reagent as per the manufacturer's protocol (Thermo Fisher Scientific). 1 week later, the cells were pelleted and discarded. The supernatants were filtered (Thermo Fisher

Scientific) (0.22-μm-pore-size filter) as directed by the manufacturer (Thermo Fisher Scientific). The supernatant containing the antibody was then passed over Protein A beads (Cytiva). Following this, the antibodies were washed, eluted and dialyzed against PBS before their concentration being measured. Antibodies were then aliquoted and stored at −80°C until further use.

SARS-CoV-2 spike ELISA (enzyme-linked immunosorbent assay)

The SARS-CoV-2 Spike ELISA assay used was recently described (Beaudoin-Bussieres et al., 2020; Prevost et al., 2020). Briefly, recombinant SARS-CoV-2 S-6P (2.5 μg/mL), or bovine serum albumin (BSA) (2.5 μg/mL) as a negative control, were prepared in PBS and were adsorbed to plates (MaxiSorp; Nunc) overnight at 4°C. Coated wells were subsequently blocked with blocking buffer (Tris-buffered saline [TBS] containing 0.1% Tween20 and 2% BSA) for 1 h at room temperature. Wells were then washed four times with washing buffer (TBS containing 0.1% Tween20). CV3-1, CV3-25, CV3-13 WT, CV3-13 LALA, CV3-13 GASDALIE and CR3022 mAbs (50 ng/mL) were prepared in a diluted solution of blocking buffer (0.1% BSA) and incubated in the coated wells for 90 min at room temperature. Plates were washed four times with washing buffer followed by incubation with HRP-conjugated anti-Human IgG secondary Abs (Invitrogen) (at a concentration of 0.267 μg/mL in a diluted solution of blocking buffer [0.4% BSA]) for 1 h at room temperature, followed by four washes. HRP enzyme activity was determined after the addition of 40 μL of a 1:1 mix of Western Lightning oxidizing and luminol reagents (Perkin Elmer Life Sciences). Light emission was measured with a LB941 TriStar luminometer (Berthold Technologies). Signal obtained with BSA was subtracted for each antibody and was then normalized to the signal obtained with CR3022 mAb present in each plate.

Flow cytometry analysis of cell-surface spike staining

10 μg of the different expressors of the original SARS-CoV-2 Spike (Hoffmann et al., 2020) or the different mutants of the SARS-CoV-2 Spike (B.1.1.7, D614G, Δ69-70, Δ144, N501Y, A570D, P681H, T716I, S982A and D1118H) (Li et al., 2021b; Prevost et al., 2021; Tauzin et al., 2021) were co-transfected with 2.5 μg of a green fluorescent protein (GFP) expressor (pIRES2-eGFP) into 2 × 10^6 293T cells using the standard calcium phosphate method. Before staining with primary antibodies, cells were washed 2 times. At 48 h post transfection, 293T cells were stained with CR3022, CV3-1, CV3-13 WT, CV3-13 LALA, CV3-13 GASDALIE and CV3-25 antibodies (5 μg/mL) for 45 min at 37°C before being washed 2 times in PBS. Alexa Fluor-647-conjugated goat anti-human IgG (H + L) Abs (Invitrogen) (2 μg/mL) and AquaVivid (Thermo Fischer Scientific) (Dilution of 1/1000) were used to stain the cells for 20 min at room temperature. The percentage of transfected cells (GFP + cells) was determined by gating the living cell population based on the basis of viability dye staining (AquaVivid, Thermo Fischer Scientific). Samples were acquired on a LSRII cytometer (BD Biosciences) and data analysis was performed using FlowJo v10.5.3 (Tree Star).

For cell surface staining of transduced CEM.NKr-Spike cells, CEM.NKr-Spike cells were stained for 45 min at room temperature with CV3-1, CV3-13 WT, CV3-13 LALA and CV3-13 GASDALIE (0.0025 μg/mL, 0.01 μg/mL, 0.05 μg/mL, 0.25 μg/mL, 1 μg/mL and 5 μg/mL) or with CV3-13 WT, CV3-13 GASDALIE, CV3-25 WT, CV3-25 LALA, 17b GASDALIE and a cocktail of 1 CV3-13 GASDALIE:1 CV3-25 LALA antibody (5 μg/mL, 2.5 μg/mL, 1.25 μg/mL, 0.625 μg/mL, 0.3125 μg/mL, 0.15625 μg/mL, 0.078125 μg/mL, 0.0390625 μg/mL, 0.0195313 μg/mL and 0.0097656 μg/mL) in PBS. Cells were then washed twice with PBS and stained with 2 μg/mL of anti-human AlexaFluor 647 (AF-647) secondary antibody and 1:1000 dilution of viability dye AquaVivid (Thermo Fisher) for 20 min in PBS at room temperature. Cells were then washed twice with PBS and fixed in a 2% PBS-formaldehyde solution. All samples were acquired on an LSRII cytometer (BD Biosciences) and data analysis was performed using FlowJo v10.5.3 (Tree Star).

Surface plasmon resonance (SPR)

All surface plasma resonance assays were performed on a Biacore 3000 (GE Healthcare) with a running buffer of 10 mM HEPES pH 7.5 and 150 mM NaCl, supplemented with 0.05% Tween 20 at 25°C. Initial epitope mapping was performed by the binding of SARS-CoV RBD (residue 306-577) and other SARS-CoV-2 antigens (S1 and S2 obtained from BEI Resources) to immobilized CV3-13 IgG (∼5800 RU) on a Protein A sensor chip (Cytiva). For the kinetic measurement of CV3-13 Fab binding to SARS-CoV-2 spike, ∼800 RU of his-tagged SARS-CoV-2 S-6P was immobilized on a Ni-pretreated NTA chip (Cytiva). 2-fold serial dilutions of purified CV3-13 Fab were then injected with concentrations ranging from 3.125 to 200 nM. Sensorgrams were corrected by subtraction of the corresponding blank channel as well as for the buffer background and kinetic constants determined using a 1:1 Langmuir model with the BIAevaluation software (GE Healthcare). Goodness of fit of the curve was evaluated by the Chi^2 of the fit with a value below 3 considered acceptable.

Pseudovirus neutralization assay

Target cells were infected with single-round luciferase-expressing lentiviral particles. Briefly, 293T cells were transfected by the calcium phosphate method with the pNL4.3 R-E− Luc plasmid (NIH AIDS Reagent Program) and a plasmid encoding for SARS-CoV-2 Spike at a ratio of 10:1. Two days post-transfection, cell supernatants were harvested and stored at −80°C until use. 293T-ACE2 (Prevost et al., 2020) target cells were seeded at a density of 1 × 10^4 cells/well in 96-well luminometer-compatible tissue culture plates (Perkin Elmer) 24 h before infection. Recombinant viruses in a final volume of 100 μL were incubated with the indicated semi-log diluted antibody concentrations (0 μg/mL, 0.01 μg/mL, 0.0316 μg/mL, 0.1 μg/mL, 0.316 μg/mL, 1 μg/mL, 3.16 μg/mL and 10 μg/mL) or with 10 μg/mL, 5 μg/mL, 2.5 μg/mL, 1.25 μg/mL, 0.625 μg/mL, 0.3125 μg/mL, 0.15625 μg/mL, 0.078125 μg/mL,

0.0390625 μg/mL and 0.0195313 μg/mL for 1 h at 37°C and were then added to the target cells followed by incubation for 48 h at 37°C; cells were lysed by the addition of 30 μL of passive lysis buffer (Promega) followed by one freeze-thaw cycle. An LB941 TriStar luminometer (Berthold Technologies) was used to measure the luciferase activity of each well after the addition of 100 μL of luciferin buffer (15 mM $MgSO_4$, 15 mM KH_2PO_4 [pH 7.8], 1 mM ATP, and 1 mM dithiothreitol) and 50 μL of 1 mM d-luciferin potassium salt.

Microneutralization assay

One day prior to infection, $2x10^4$ Vero E6 cells were seeded per well of a 96 well flat bottom plate and incubated overnight to permit Vero E6 cell adherence. Antibody concentrations (0 μg/mL, 0.01 μg/mL, 0.0316 μg/mL, 0.1 μg/mL, 0.316 μg/mL, 1 μg/mL, 3.16 μg/mL and 10 μg/mL) were performed in a separate 96 well culture plate using DMEM supplemented with penicillin (100 U/mL), streptomycin (100 μg/mL), HEPES, 0.12% sodium bicarbonate, 2% FBS and 0.24% BSA. 10^4 $TCID_{50}$/mL of authentic SARS-CoV-2 D614G virus (derived from strain LSPQ/231457/2020 (Prevost et al., 2021)) was prepared in DMEM + 2% FBS and combined with an equivalent volume of diluted antibodies for one hour. After this incubation, all media was removed from the 96 well plate seeded with Vero E6 cells and virus:antibody mixture was added to each respective well at a volume corresponding to 600 $TCID_{50}$ per well and incubated for one hour further at 37°C. Both virus only and media only (MEM + 2% FBS) conditions were included in this assay. All virus:antibody supernatant was removed from wells without disrupting the Vero E6 monolayer. Each diluted antibody (for a volume of 100 μL) was added to its respective Vero E6-seeded well in addition to an equivalent volume of MEM + 2% FBS and was then incubated for 48 h. Media was then discarded and replaced with 10% formaldehyde for 24 h to cross-link Vero E6 monolayer. After, formaldehyde was removed from wells and subsequently washed with PBS. Cell monolayers were permeabilized for 15 min at room temperature with PBS + 0.1% Triton X-100, washed with PBS and then incubated for one hour at room temperature with PBS + 3% non-fat milk. A mouse anti-SARS-CoV-2 nucleocapsid protein monoclonal antibody (Clone 1C7, Bioss Antibodies) solution was prepared at 1 μg/mL in PBS + 1% non-fat milk and added to all wells for one hour at room temperature. Following extensive washing (3×) with PBS, an anti-mouse IgG HRP secondary antibody solution was formulated in PBS + 1% non-fat milk. One hour post-room temperature incubation, wells were washed with 3×PBS, substrate (ECL) was added and an LB941 TriStar luminometer (Berthold Technologies) was used to measure the signal each well.

Cell-surface staining of SARS-CoV-2-infected cells

8M Vero-E6 cells were plated in T-175 flask 24 h before infection. Authentic SARS-CoV-2 virus (MOI = 0.01) was used for infection. After 48 h, infected Vero E6 cells were detached with PBS-EDTA and were incubated with 5 μg/mL of indicated antibodies for 30 min at 37°C, followed by staining with anti-human –AF647 secondary antibody and 1:1000 dilution of viability dye AquaVivid (Thermo Fisher Scientific) for 20 min at room temperature. Cells were then treated with 4% PFA for 24 h at 4°C. Then the cells were stained intracellularly for SARS-CoV-2 nucleocapsid (N) antigen, using the Cytofix/Cytoperm fixation/permeabilization kit (BD Biosciences) and an anti-N mAb (clone mBG17; Kerafast) conjugated with the Alexa Fluor 488 dye according to the manufacturer's instructions (Invitrogen). The percentage of infected cells (N+ cells) was determined by gating the living cell population based on the basis of viability dye staining (Aqua Vivid, Invitrogen). Samples were acquired on a LSRII cytometer (BD Biosciences, Mississauga, ON, Canada) and data analysis was performed using FlowJo v10.5.3 (Tree Star, Ashland, OR, USA).

Cryo-immunohistology of organs

Organs were isolated after necropsy and fixed in 1X PBS containing freshly prepared 4% PFA for 12 h at 4°C. They were then washed with PBS, cryoprotected with 10, 20 and 30% ascending sucrose series, snap-frozen in Tissue-Tek® O.C.T.™ compound and stored at −80°C. 10 μm thick frozen sections were permeabilized with 0.2% Triton X-100 and treated with Fc receptor blocker (Innovex Biosciences) before staining with indicated conjugated primary, secondary antibodies in PBS containing 2% BSA containing 10% fetal bovine serum. Stained sections were treated with TrueVIEW Autofluorescence Quenching Kit (Vector Laboratories) and mounted in VECTASHIELD® Vibrance™ Antifade Mounting Medium. Images were acquired using Nikon W1 spinning disk confocal microscope equipped with 405, 488, 561 and 647 nm laser lines or EVOS M7000 imaging system. The images were processed using Nikon Elements AR version 4.5 software (Nikon Instruments Inc, Americas) and figures assembled with Photoshop CC and Illustrator CC (Adobe Systems, San Jose, CA, USA).

Antibody dependent cellular cytotoxicity (ADCC) assay

This assay was previously described (Anand et al., 2021; Beaudoin-Bussieres et al., 2021). Briefly, for evaluation of anti-SARS-CoV-2 ADCC activity, parental CEM.NKr CCR5+ cells were mixed at a 1:1 ratio with CEM.NKr-Spike cells. These cells were stained for viability (AquaVivid; Thermo Fisher Scientific) and a cellular dye (cell proliferation dye eFluor670; Thermo Fisher Scientific) and subsequently used as target cells. Overnight rested PBMCs were stained with another cellular marker (cell proliferation dye eFluor450; Thermo Fisher Scientific) and used as effector cells. Stained effector and target cells were mixed at a 10:1 ratio in 96-well V-bottom plates. Titrated concentrations of CV3-1, CV3-13 WT, CV3-13 LALA and CV3-13 GASDALIE, CV3-25 WT, CV3-25 LALA, 17b GASDALIE and a cocktail of 1 CV3-13 GASDALIE:1 CV3-25 LALA (0.0025 μg/mL, 0.01 μg/mL, 0.05 μg/mL, 0.25 μg/mL, 1 μg/mL and 5 μg/mL or 5 μg/mL, 2.5 μg/mL, 1.25 μg/mL, 0.625 μg/mL, 0.3125 μg/mL, 0.15625 μg/mL, 0.078125 μg/mL, 0.0390625 μg/mL, 0.0195313 μg/mL and 0.0097656 μg/mL) were added to the appropriate wells. The plates were subsequently centrifuged for 1 min at 300 x g, and incubated at 37°C, 5% CO_2 for 5 h before being fixed in a 2%

PBS-formaldehyde solution. Since CEM.NKr-Spike cells express GFP, ADCC activity was calculated using the formula: [(% of GFP + cells in Targets plus Effectors) - (% of GFP + cells in Targets plus Effectors plus antibody)]/(% of GFP + cells in Targets) x 100 by gating on transduced live target cells. All samples were acquired on an LSRII cytometer (BD Biosciences) and data analysis performed using FlowJo v10.5.3 (Tree Star).

Antibody dependent cellular phagocytosis (ADCP) assay

The ADCP assay was performed using CEM.NKr-Spike cells as target cells that were fluorescently labelled with a cellular dye (cell proliferation dye eFluor450). THP-1 cells were used as effector cells and were stained with another cellular dye (cell proliferation dye eFluor670). Stained target cells were incubated with 100 μL of the titrated concentrations of CV3-1, CV3-13 WT, CV3-13 LALA and CV3-13 GASDALIE antibodies (0,625 μg/mL, 1,25 μg/mL, 2,5 μg/mL, 5 μg/mL and 10 μg/mL) for 1 h at 37°C, followed by two washes with media. Stained target and effector cells were mixed at a 5:1 ratio in 96-well U-bottom plates. After a 5 h incubation at 37°C and 5% CO_2, cells were fixed with a 2% PBS-formaldehyde solution. Antibody-mediated phagocytosis was determined by flow cytometry, gating on THP-1 cells that were triple-positive for eFluor450 and eFluor670 cellular dyes and GFP. All samples were acquired on an LSRII cytometer (BD Biosciences) and data analysis performed using FlowJo v10.5.3 (Tree Star).

Cryo-EM sample preparation and data collection

SARS-CoV-2 HexaPro spike (GnT1-produced) was incubated with 20-fold excess of CV3-13 Fab overnight at 4°C before purification on a Superose 6 300/10 GL column (GE Healthcare). The complex peak was harvested, concentrated to 0.50 mg/mL in the SEC buffer and immediately used for Cryo-EM grid preparation. 3 μL of protein was deposited on a holey copper grids (QUANTIFOIL R 1.2/1.3, 200 mesh, EMS) which had been glow-discharged for 30 s at 15 Ma using PELCO easiGlow (TedPella Inc). Grids were vitrified in liquid ethane using Vitrobot Mark IV (Thermo Fisher) with a blot time of 2–4 s and variable blot force at 4°C and 100% humidity.

The frozen grids were screened on a FEI Talos Arctica microscope at 200 kV equipped with a FEI Falcon3EC detector using the EPU software (Thermo Fisher). Cryo-EM data from a good grid were acquired on a FEI Glacios electron microscope operating at 200 kV, equipped with a Gatan K3 direct electron detector. Micrographs were collected at a magnification of 45,000 corresponding to a calibrated pixel size of 0.8893 Å, with a total exposure dose of 42 $e^-/Å^2$.

Cryo-EM data processing, model building and analysis

Motion correction, CTF estimation, particle picking, curation and extraction, 2D classification, *ab initio* model reconstruction, volume refinements and local resolution estimation were carried out in cryoSPARC (Punjani et al., 2017; Rubinstein and Brubaker, 2015). An initial SARS-CoV-2 spike model (PDB: 6XKL) with single-RBD up and a three-RBD-down (closed) model (PDB: 6VXX) were used as modeling templates. The NTDs were initially modelled from PDB entry 7C2L. The initial models for CV3-13 Fab were generated in the SAbPred server (Dunbar et al., 2016) using the primary sequence.

Automated and manual model refinements were iteratively carried out in ccpEM (Burnley et al., 2017), Phenix (Liebschner et al., 2019) (real-space refinement) and Coot (Emsley and Cowtan, 2004). Geometry validation and structure quality evaluation were performed by EM-Ringer (Barad et al., 2015) and Molprobity (Chen et al., 2010). Model-to-map fitting cross correlation and figures generation were carried out in USCF Chimera, Chimera X (Pettersen et al., 2021) and PyMOL (The PyMOL Molecular Graphics System, Version 1.2r3pre, Schrödinger, LLC). The complete cryo-EM data processing workflow is shown in Figure S4, statistics of data collection, reconstruction and refinement is described in Table S1 and structure is deposited in the Protein Data Bank (PDB) with accession code 7RQ6. The epitope interface analysis was performed in PISA (Krissinel and Henrick, 2007).

QUANTIFICATION AND STATISTICAL ANALYSIS

Statistical significance was derived by applying parametric unpaired t test or non-parametric Mann-Whitney U test (two-tailed) available in GraphPad Prism software (La Jolla, CA, USA) depending on the normality distribution of the data. *p* values lower than 0.05 were considered statistically significant. p values were indicated as *, $p < 0.05$; **, $p < 0.01$; ***, $p < 0.001$; ****, $p < 0.0001$.